§

CRI-HOM: A novel chemical mechanism for simulating Highly Oxygenated Organic Molecules (HOMs) in global chemistry-aerosol-climate models.

James Weber[1], Alexander T. Archibald[1,2], Paul Griffiths[1,2], Scott Archer-Nicholls[1], Torsten Berndt[3], Michael Jenkin[4], Hamish Gordon[5], Christoph Knote[6]

[1]Centre for Atmospheric Science, Department of Chemistry, University of Cambridge, Cambridge, CB2 1EW, UK
[2]National Centre for Atmospheric Science, Department of Chemistry, University of Cambridge, CB2 1EW, UK
[3]Atmospheric Chemistry Department (ACD), Leibniz Institute for Tropospheric Research (TROPOS), Leipzig, 04318, Germany
[4]Atmospheric Chemistry Services, Okehampton, Devon, UK
[5]College of Engineering, Carnegie Mellon University, Pittsburgh, PA 15213, USA
[6]Meteorologisches Institut, Ludwig-Maximilians-Universität München, Munich, 80333, Germany

Correspondence to: James Weber (jmw240@cam.ac.uk)

Abstract.

We present here results from a new mechanism, CRI-HOM, which we have developed to simulate the formation of highly oxygenated organic molecules (HOMs) from the gas phase oxidation of α-pinene, one of the most widely emitted BVOCs by mass. This concise scheme adds 12 species and 66 reactions to the Common Representative Intermediates (CRI) mechanism v2.2 Reduction 5 and enables the representation of semi-explicit HOM treatment suitable for long term global chemistry-aerosol-climate modelling, within a comprehensive tropospheric chemical mechanism. The key features of the new mechanism are (i) representation of the autoxidation of peroxy radicals from the hydroxyl radical and ozone initiated reactions of α-pinene, (ii) formation of multiple generations of peroxy radicals, (iii) formation of accretion products (dimers) and (iv) isoprene-driven suppression of accretion product formation, as observed in experiments. The mechanism has been constructed through optimisation against a series of flow tube laboratory experiments. The mechanism predicts a HOM yield of 4-6% under conditions of low to moderate NOx, in line with experimental observations, and reproduces qualitatively the decline in HOM yield and concentration at higher NOx. The mechanism gives a HOM yield that also increases with temperature, in line with observations, and our mechanism compares favourably to some of the limited observations of [HOM] observed in the boreal forest in Finland and in the south east USA.

The reproduction of isoprene-driven suppression of HOMs is a key step forward as it enables global climate models to capture the interaction between the major BVOC species, along with the potential climatic feedbacks. This suppression is demonstrated when the mechanism is used to simulate atmospheric profiles over the boreal forest and rainforest; different isoprene concentrations result in different [HOM] distributions, illustrating the importance of BVOC interactions in atmospheric composition and climate. Finally particle nucleation rates calculated from [HOM] in present day and pre-industrial atmospheres suggest that "sulphuric acid free" nucleation can compete effectively with other nucleation pathways in the boreal forest, particularly in the pre-industrial, with important implications for the aerosol budget and radiative forcing.

1 Introduction

Aerosols play an important role in the Earth system by affecting the Earth's radiative balance as well as local air quality and thus human health (Carslaw et al., 2010). Aerosols can interact directly with solar radiation through scattering or absorption

§

and indirectly by influencing cloud properties by seeding cloud droplets as well as increasing cloud albedo (Forster et al., 2007, Twomey., 1974). Thus, aerosols change the balance between the energy received from the Sun and the energy emitted from the planet at the top of the atmosphere. However, a major uncertainty in climate change predictions arises from aerosols and aerosol-cloud interactions (Stocker et al., 2014). This arises in part from a lack of understanding of pre-
45   industrial (PI) aerosol and it is the change in aerosol burden from the PI to the present day (PD) which determines the effective radiative forcing (ERF) of aerosols. As PI aerosols sources are almost exclusively natural, an understanding of natural sources and the associated aerosol formation processes is essential if better predictions for climate change are to be made.

50   An important formation route for aerosols is oxidation of volatile organic compounds which form less volatile species that can partition into the aerosol phase or nucleate new particles (Kirkby et al., 2016, Shrivastava et al., 2017). Recently it has been established that the oxidation of organic compounds can lead to the formation of "highly oxygenated organic molecules" (HOMs) (Bianchi et al., 2019) (also referred to as "highly oxidised multifunctional organic compounds (Ehn et al., 2012)) which are formed by multiple intramolecular oxidation steps, termed autoxidation (Crounse et al., 2013, Bianchi
55   et al., 2019). Autoxidation typically involves the abstraction by a peroxy radical of a hydrogen atom bonded to a carbon elsewhere on the molecule resulting in an alkyl radical and hydroperoxide group. The alkyl radical reacts rapidly with atmospheric oxygen to form a new peroxy radical, ultimately reducing the species' volatility and enabling particle formation/condensation. HOMs are defined as closed-shell species with at least 6 oxygens formed by initial atmospheric oxidation and subsequent autoxidation steps (Bianchi et al., 2019). HOM formation has been observed from anthropogenic
60   species (Berndt et al., 2018a) and biogenic species such as α-pinene (Molteni et al., 2019, Berndt et al., 2018b). The semi-explicit mechanism described for the first time in this paper describes the formation of HOMs from α-pinene in a form suitable for global modelling studies. This provides a framework for incorporating a comprehensive description of pure biogenic nucleation into a global model and, ultimately, allowing for a more rigorous description of aerosol formation and the climatic consequences. α-pinene is considered as it is the most widely studied and widely emitted monoterpene (~32 Tg
65   yr^{-1}, Sindelarova et al., 2014) and, with measured HOM yields around 3-10 % (Ehn et al., 2014, Jokinen et al. 2015), has the potential to produce 2-7 Tg HOM yr^{-1} with the range arising from uncertainties in emissions, HOM yield and difference in mass between the precursor BVOC and the HOMs which will have at least 6 additional oxygen atoms but in some cases, considerably more. HOM yields from β-pinene (the second most widely emitted monoterpene, Sindelarova et al., 2014) and isoprene (the most widely emitted BVOC, Sindelarova et al., 2014) are negligible (Ehn et al., 2014). Limonene has
70   emissions around 25% of α-pinene (Sindelarova et al., 2014) and is likely to have a higher HOM yield (Ehn et al., 2014, Jokinen et al., 2015) although a much wider range of values have been reported than for α-pinene. Limonene thus may have the potential to produce a similar mass of HOM as α-pinene and its consideration may be an area of future work. Emissions of anthropogenic VOCs account for ~10% of total VOC emissions (Guenther et al., 1995), roughly the same quantity as monoterpene emissions, and, as no species have HOM yields above 2.5% (Bianchi et al., 2019), the contribution of
75   anthropogenic VOCs to HOM is likely to be significantly smaller. Nevertheless, the speciation of anthropogenic VOCs in the mechanism means that addition of HOMs from these sources will be possible and, from an urban air quality perspective very important.

Nucleation of new particles from sulphuric acid is an important means of new particle formation (NPF) in the atmosphere
80   (Kulmala et al., 1998). Sulphuric acid can also form new particles with oxidised organic species (Riccobono et al., 2015). However, extremely involatile HOMs can participate in NPF, without necessarily needing a sulphuric acid seed in a process termed pure biogenic nucleation (PBN) (Kirkby et al., 2016, Gordon et al., 2016). Despite playing important roles in aerosol

Atmospheric
Chemistry
and Physics
Discussions

§

formation and growth, the relatively recent discovery of HOMs and the complexity of their formation means that their role in particle formation and contribution to aerosol has been assessed in only very few global model studies (Gordon et al., 2016,
85 Zhu et al., 2019). The ability of PBN to change atmospheric aerosol loading by providing a route to particle formation without sulphuric acid has been illustrated (Gordon et al., 2016) with this effect particularly important in the pre-industrial (PI) atmosphere, where lower SO_2 emissions resulted in greater sensitivity of aerosol loading to alternative formation routes (i.e. including PBN) and a higher simulated aerosol burden than previous studies. As a result, Gordon et al (2016) calculated that the radiative forcing change from the PI to PD caused by cloud cover change was 27% lower than previous estimates.
90 Meanwhile, Zhu et al (2019), highlighting the fact that many chemistry schemes fail to reproduce nucleation rates in low sulphuric acid concentrations, showed the complex effect PBN has in the PI and PD with a more complicated mechanism but one which also omitted autoxidation and accretion product formation. Including PBN in a global chemistry-aerosol scheme resulted in a much larger increase in the magnitude of the (negative) aerosol indirect effect (AIE) in the PI than the PD. This has potentially important consequences as it means that the effective radiative forcing (ERF) of aerosols from the PI to PD
95 may be smaller than previously expected. This in turn would mean that climate sensitivity is lower than previously thought as aerosols are offsetting a smaller amount of warming arising from the enhanced concentrations of greenhouse gases than previously thought, with implications for predictions of future climate change as well.

The peroxy radicals produced from α-pinene oxidation by OH or O_3 have been observed to undergo autoxidation under
100 typical atmospheric conditions (Ehn et al., 2014, Jokinen et al., 2014, Berndt et al., 2016, Berndt et al., 2018b). The autoxidation competes with the bimolecular reaction of peroxy radicals with NO, NO_3, HO_2 and other peroxy radicals and its yield is thus dependent on background atmospheric composition. Therefore, an accurate description of HOMs requires consideration of NO_x and oxidant concentrations as well as autoxidation; indeed elevated NO_x has been observed to suppress HOM formation (Lehtipalo et al., 2018). The first order rate constants for autoxidation can vary over several orders of
105 magnitude ($\sim 10^{-6} - 10^2$ s^{-1}) depending on nearby functional groups (Bianchi et al., 2019, Crounse et al., 2013, Xu et al., 2018, Kurten et al., 2015). Autoxidation rates also exhibit a significant positive temperature dependence (Jenkin et al., 2019a, Bianchi et al., 2019) and HOM yield has been observed to be highly temperature dependent (Quéléver et al., 2019). Thus, the overall competitiveness of autoxidation is dependent on the background atmospheric composition and ambient temperature as well as the molecule undergoing oxidation.
110

In addition to autoxidation, the formation of HOM accretion products (also called dimers (Kurten et al., 2016, Bianchi et al., 2019)) by reactions between two peroxy radicals has been observed to be significant with large peroxy radicals (Kirkby et al., 2016, Berndt et al., 2018a, Berndt et al., 2018b, Jenkin et al., 2019a, Molteni et al., 2019). These species are predicted to be more involatile than 10-carbon HOMs (also termed monomers (Kurten et al., 2016)) with important implications for new
115 particle formation and contribution to SOA. In established schemes such as the Master Chemical Mechanism (MCM) (Jenkin et al., 1997, Saunders et al., 2003), the Common Representative Intermediates (CRI) (Utembe et al., 2010, Watson et al., 2010, Jenkin et al., 2010, Jenkin et al., 2019) and the Chemistry of the Stratosphere and Troposphere (Strat-Trop) used in the climate model UKCA (United Kingdom Chemistry and Aerosol) (Archibald et al., 2019), formation of accretion products is not included as it was previously considered negligible or too complex to include. However, experimental work suggests that accretion product formation is a competitive pathway for larger peroxy radicals, such as those formed from α-
120 pinene (Berndt et al., 2018b, Molteni et al., 2019) and indeed becomes more favourable with increasing functionality and size; the rate coefficient for the accretion reaction between two α-pinene derived peroxy radicals was observed to be 16-80 times greater (depending on the extent of oxidation) than for the analogous reaction between two isoprene derived peroxy radicals (Berndt et al., 2018a, Berndt et al., 2018b).
125

§

The mechanistic treatment of HOMs in numerical models has varied considerably from simple steady state approximations (Gordon et al., 2016) through basic mechanisms linked to a volatility basis set (Schervish et al., 2019) to more explicit descriptions based on the MCM featuring either a limited subset of HOMs without accretion product formation or autoxidation (Zhu et al., 2019) or a near explicit description involving over 1700 reactions (Roldin et al., 2019). Whilst the

130 addition of PBN represents an important process level improvement in models, the approaches discussed above all have some degree of limitation. As well as omitting accretion product formation, simpler models (Gordon et al., 2016, Schervish et al., 2019) do not fully capture the influence of oxidant levels, NO_x or temperature while the more explicit schemes (Zhu et al., 2019, Roldin et al., 2019) are too computationally expensive for long term climate studies. Further, none of the schemes include the relatively novel observation of suppression via reactive RO_2 cross reactions (McFiggans et al., 2019), although

135 this has been identified as an important area for future research (Zhu et al., 2019, Roldin et al., 2019) and is addressed in this work.

New experimental evidence suggests that isoprene may suppress the formation of the most involatile accretion products and thus the smallest aerosol particles (Berndt et al 2018b, McFiggans et al., 2019) and reproducing the effect of isoprene has

140 been identified as an important requirement for future mechanisms (Roldin et al., 2019). This inhibition is driven firstly by isoprene scavenging OH radicals (Lee et al., 2016, Kiendler-Scherr et al., 2009, Berndt et al, 2018b) thus reducing the formation of large peroxy radicals by reaction of α-pinene with OH. The second driver is the scavenging of the 10-carbon α-pinene peroxy radicals ("C10RO2) by isoprene peroxy radicals ("C5RO2") and the other smaller peroxy radicals from species such as CO and CH_4 (McFiggans et al., 2019). These C10RO2 could otherwise form 20-carbon accretion products

145 (Eq. 1) which are predicted to be highly involatile (Kurten et al., 2016). The reaction of isoprene peroxy radicals with the α-pinene radicals produces the 15-carbon accretion product ("C15d") (Eq. 2) as well as closed shell species ("C10" and "C5") (Eq. 3) and alkoxy radicals ("C10RO" and "C5RO") (Eq. 4) which isomerise or fragment (Jenkin et al, 2019a).

$$C10RO_2 + C10RO_2 \rightarrow C20d + O_2 \ (1)$$

150

$$C10RO_2 + C5RO_2 \rightarrow C15d + O_2 \ (2)$$

$$C10RO_2 + C10RO_2 \rightarrow C10 + C5 + O_2 \ (3)$$

155 $$C10RO_2 + C10RO_2 \rightarrow C10RO + C5RO + O_2 \ (4)$$
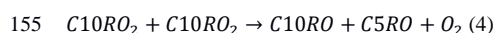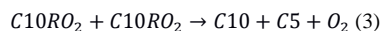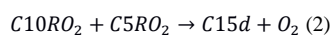
This inhibition affects the aerosol size distribution (an important parameter for the radiative forcing of aerosol (Zhu et al., 2019)) by favouring the growth of larger existing aerosol particles by promoting the production of smaller, more volatile species which can partition to pre-existing aerosol rather than the nucleation of new particles from larger, less volatile

160 species. This has the potential to have important consequences for future predictions of SOA and the negative feedback proposed to exist between biogenic VOC emissions and atmospheric temperature (Kulmala et al., 2004, Carslaw et al., 2010, Sporre et al., 2018). Such predictions, based on the modelled increases in isoprene and monoterpene emissions in a warmer climate (Kulmala et al., 2013, Sporre et al., 2018) have not considered the potential perturbation to NPF and atmospheric aerosol loading by isoprene and the changes in radiative forcing which may result. Reassessing the sign and size of this

165 feedback by coupling the chemistry scheme described in this work to an aerosol scheme within a global climate models is a key long-term aim of this work.

§

In this study we describe our work developing a new mechanism sufficiently concise for global chemistry climate models that can simulate the process of autoxidation, the formation of HOMs from α-pinene and the influence of isoprene. In Section 2 the development of the mechanism from the principles of gas phase chemistry is described and in Section 3 we discuss mechanism optimisation and validation against experimental data and the parent mechanism, CRI v2.2. In Section 4, the mechanism is used to simulate atmospheric HOM profiles and explore implications for new particle formation. Finally, in Section 5, conclusions for further work are drawn.

2 Mechanism Development

Our new mechanism we have developed builds on the Common Representative Intermediates (CRI) scheme version 2.2 Reduction 5 (Jenkin et al., 2019b) (hereafter the "base mechanism"), developed from the fully explicit Master Chemical Mechanism (MCM) version 3.3.1 (Jenkin et al., 2015) which describes the degradation of organic compounds in the troposphere. In the CRI framework, species are lumped together into surrogate molecules whose behaviour is optimised against the fully explicit MCM. The CRI v2.2 R5 mechanism describes the degradation of α-pinene, β-pinene, isoprene and 19 other emitted VOC species.

The updates we have made to the base mechanism to produce the new HOM-forming functionality include the addition of autoxidation of α-pinene oxidation products and a more detailed peroxy radical pool scheme. These changes enable the formation of 10-carbon, 15-carbon and 20-carbon HOMs and add 12 species and 66 reactions to the base mechanism. The new chemical mechanisms for ozonolysis and OH oxidation are shown in Figure 1 and Figure 2 respectively. We now describe the changes made to the base mechanism to incorporate HOM chemistry in more detail.

2.1 Ozonolysis

To simulate the autoxidation reactions formed from ozonolysis 5 new peroxy radical species were added to the base mechanism. The peroxy radicals formed from ozonolysis of α-pinene and subsequent autoxidation steps are collectively termed "O3RO2". In the base mechanism, α-pinene reacts with ozone to produce the single lumped peroxy radical RN18AO2 and acetone. This single mechanistic step represents multiple chemical steps, with RN18AO2 representing a 6 or 7 carbon species. In addition, TNCARB26 (closed shell carbonyl species) and RCOOH25 (pinonic acid) arise from the reaction of Criegee intermediates with water. RN18AO2 goes on to react with standard peroxy radical reaction partners; HO_2 forming hydroperoxides; NO and NO_3 forming alkoxy radicals; and the peroxy radical pool forming alkoxy radicals, carbonyls and alcohols, as described in (Jenkin et al., 2019a).

In our new mechanism, RN18AO2 is replaced with the tracers RN26BO2 and RTN24BO2. RN26BO2 represents the 10-carbon peroxy radicals formed directly from the cleavage of the ozonide and subsequent addition of atmospheric oxygen, which can then undergo autoxidation. RTN24O2, a species already in the CRI mechanism, represents the 9 carbon peroxy radical species (MCM species C96O2) which is also formed from ozonolysis but does not undergo autoxidation in this mechanism. RN26BO2 is termed "1st generation" as it has undergone one oxidation step and it can undergo autoxidation to form the 2nd, 3rd, 4th and lumped higher generation species, termed RN25BO2O2, RN24BO4O2, RN23BO4O2 and RNxBOyO2 species respectively (RNxBOyO2 does not undergo further autoxidation but does undergo all the other reactions). In the base mechanism, the first number featured in a species' name is an index which refers to the number of NO-to-NO_2 conversions possible, which depends on the number of C-C and C-H bonds. During the H-shift step of autoxidation, a C-H bond is usually broken to produce the alkyl radical which then forms the peroxy radical from

Atmospheric
Chemistry
and Physics
Discussions

§

atmospheric oxygen and so each autoxidation step reduces the index by one while the number of oxygens is increased by 2.

210 For example, the autoxidation of the 2nd generation O3RO2 to 3rd generation is expressed by Eq.5.

$$RN25BO2O2 \rightarrow RN24BO4O2 \text{ (5)}$$
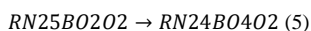
Each generation of peroxy radical also undergoes bimolecular reactions. Reaction with HO$_2$ produces a hydroperoxide species; for the 2nd and later generations, the product is classified as a HOM (C10z) as they fulfil the criteria discussed by Bianchi et al (2019), while for the 1st generation species the resulting hydroperoxide is RTN26OOH, a species already

215 present in the CRI (Eq. 6).

$$RNaBObO2 + HO_2 \rightarrow RTN26OOH \text{ or } C10z \text{ (6)}$$

Reaction with NO and NO$_3$ yields nitrates or alkoxy radicals and accurately representing the behaviour of these products is crucial to reproducing the effect of NO$_x$ on HOM formation. Alkoxy radicals are not represented explicitly due to their rapid

220 reactions which, typically for larger peroxy radicals, are decomposition or isomerisation. Decomposition produces two smaller species, one closed shell and one a peroxy radical while isomerisation produces a more functionalised peroxy radical via an alkyl radical intermediate with one fewer oxygen than would have been added via autoxidation. Faced with very limited data and the fact that the precise fate of an alkoxy radical will depend considerably on molecular structure and neighbouring groups, a branching ratio 50:50 for decomposition and isomerisation was adopted. The decomposition products

225 are existing CRI species CARB16 and RN10O2 or RN9O2 and the isomerisation product the next generation peroxy radical as shown in the example reaction (Eq. 7).

$$RN25BO2O2 + NO \rightarrow 0.5RN24BO4O2 + 0.5CARB16 + 0.5RN9O2 \text{ (7)}$$

A schematic of the additions made to the CRI for the ozonolysis scheme is shown in Figure 1.

230 **2.2 OH oxidation**

Autoxidation through the OH initiated oxidation pathway resulted in the addition of 6 new species, including 5 new peroxy radicals. The peroxy radicals formed from OH oxidation of α-pinene and subsequent autoxidation steps are termed "OHRO2". The single peroxy radical RTN28O2 in the base mechanism is replaced by RTN28AO2, representing the two species which do not undergo autoxidation (APINAO2 and APINBO2 in the MCM), and RTN28BO2 (MCM APINCO2)

235 which can undergo autoxidation to form higher generation peroxy radicals (Xu et al., 2018). The 2nd and 3rd generation OHRO2 are represented explicitly (RTN27BO2O2 and RTN26BO4O2) and all 4th generation and higher species are lumped together as RTNxBOyO2 for mechanistic simplicity. The chemical treatment of RTN28AO2 is the same as the original CRI species RTN28O2 while all other OHRO2 (except RTNxBOyO2) can undergo autoxidation (Eq. 8).

240 $$RTNaBObO2 \rightarrow RTN(1-a)BO(b+2)O2 \text{ (8)}$$

Reaction of the 1st and 2nd generation OHRO2 (RTN28BO2 and RTN27BO2O2) with HO$_2$ yields the hydroperoxide RTN28OOH which is not classified as a HOM due to insufficient oxygens. All later generations OHRO2 produce the HOM species C10x (Eq. 9).

245

$$RTNaBObO2 + HO_2 \rightarrow RTN28OOH \text{ or } C10z \text{ (9)}$$

§
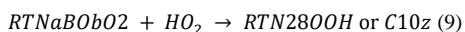
Reaction with NO and NO$_3$ is treated in the same manner as O3RO2 except for RTN28BO2 which follows the reaction of the analogous species APINCO2 in the MCM. A schematic of the additions made to the base mechanism for the OH

250   oxidation scheme is shown in Fig. 2.

The pathway initiated by reaction of α-pinene with NO$_3$ was not considered in this work but is identified as an area for future work. A summary of the peroxy in the two pathways is given in Table 1 and full mechanistic description provided in the SI.

2.3 Peroxy Radical + Peroxy Radical Interactions

255   Reactions between peroxy radicals can result in the formation of two alkoxy radicals (Eq. 10), a carbonyl and an alcohol (Eq. 11) or accretion product (Eq. 12) (Jenkin et al., 2019a).

$$RO_2 \ + \ R'O_2 \ \rightarrow \ RO \ + \ R'O \ + \ O_2 \ (10)$$

$$RO_2 \ + \ R'O_2 \ \rightarrow \ R_{-H}O \ + \ R'OH \ + \ O_2 \ \text{or} \ R'_{-H}O \ + \ ROH \ + \ O_2 \ (11)$$

260

$$RO_2 \ + \ R'O_2 \ \rightarrow \ ROOR' \ + \ O_2 \ (12)$$
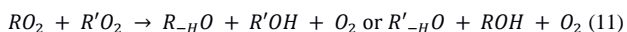
Rather than represent every possible RO$_2$-RO$_2$ reaction combination, the base mechanism uses a peroxy radical pool. Each peroxy radical undergoes a unimolecular reaction with a first order rate coefficient determined by the total peroxy radical

265   concentration and the geometric mean of the self-reaction rates of the methyl peroxy radical and radical of interest (Jenkin et al., 2019a).

While computationally efficient, such a mechanism fails to represent the effect of peroxy radical size on the distribution of products. While negligible for small peroxy radicals, accretion product formation is more favourable when larger, more

270   functionalised peroxy radicals react (Berndt et al., 2018b, Schervish et al., 2019). To describe the reactions between the differently sized peroxy radicals, we have split the single peroxy radical pool into three pools for small (<4 carbons), medium (4-7 carbons) and big (>7 carbons) peroxy radicals. Each big and medium peroxy radical reacts separately with each peroxy radical pool while, to minimise the total number of reactions, all small peroxy radicals react with the total pool as accretion product formation is much less favourable (Jenkin et al., 2019). The use of large and medium peroxy radical pools

275   allows for improved representation of the competition between peroxy radicals with different reactivity in our new mechanism and is a substantial improvement over the base mechanism.

Table 2 summarises the products for a specific peroxy radical reacting with the different peroxy radical pools. As discussed previously, alkoxy radials were not simulated explicitly, rather they decomposed into closed shell products and peroxy

280   radicals. A full list of the contents of each peroxy radical pool is given in the SI.

In practice, the alkoxy radicals formed from the reaction of isoprene-derived peroxy radicals (which are likely to dominate the medium size pool) with other peroxy radicals decompose rapidly into the major products; closed shell carbonyls methyl vinyl ketone and methacrolein (UCARB10) and the minor product hydroxy vinyl carbonyl (UCARB12) (Jenkin et al., 2015).

285   The accretion of isoprene-derived peroxy radicals has been measured to be over an order of magnitude slower than the accretion of peroxy radicals derived from α-pinene (Berndt et al., 2018b), supporting the theory that accretion product

§

formation becomes more favourable with increasing peroxy radical size. Therefore, to limit complexity, all me peroxy radicals in the mechanism simply react with the overall peroxy radical pool and their accretion product formation was ignored.

290

2.3.1 Large Peroxy Radical Pool

The reaction of a large peroxy radical with the large peroxy radical pool ($RO2_b$) can produce an accretion product (Eq. 13), closed species (Eq. 14) or an alkoxy radical (Eq. 15) (Jenkin et al., 2019a) which then reacts as discussed in sections 2.1 and 2.2. Note that a single C10RO2 species will produce half a C20d accretion product for the purposes of mass conservation.

295

$$C10RO_2 + RO2_b \rightarrow 0.5 C20d + O_2 : k_{13} \ (13)$$

$$C10RO_2 + RO2_b \rightarrow C10z/C10x/TNCARB\,26 : k_{14} \ (14)$$

300 $$C10RO_2 + RO2_b \rightarrow C10RO : k_{15} \ (15)$$
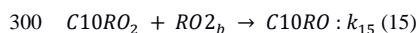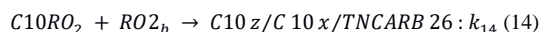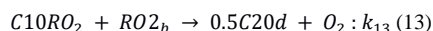
The rate coefficient for C20d formation, k_{13}, increased with the extent of oxidation of the reacting peroxy radical. This was done to simulate the observed behaviour that accretion product formation becomes faster as the reacting peroxy radicals become more functionalised (Berndt et al., 2018a, Berndt et al., 2018b). The fitting of k_{13} rate coefficients to experimental 305 data is discussed in Section 3.1.3. The chosen fitted values of 0.4-3.6×10^{-11} cm^3 molecule^{-1} s^{-1} were in line with the range measured by Berndt et al (2018b) (0.97-7.9×10^{-11} cm^3 molecule^{-1} s^{-1}) and resulted in R13 being more important that R14 and R15 which had rate coefficients based on literature (MCM, Jenkin et al., 2019a) up to an order of magnitude lower.

The rate coefficient for the formation of the closed shell species from O3RO2, k_{14}, was taken as the mean of the rate 310 coefficients measured by Molteni et al (2018) (1.68×10^{-12} cm^3 molecule^{-1} s^{-1}). The rate coefficient for alkoxy radical formation, k_{15}, was assumed to have the same value as k_{14} (i.e. a 50:50 branching ratio between these pathways).

The rate coefficients for formation of closed shell species and alkoxy radicals from OHRO2 with $RO2_b$ were taken from Roldin et al (2019).

315

2.3.2 Medium and Small Peroxy Radical Pools

Reaction of a large peroxy radical with the medium peroxy radical pool ($RO2_m$) can produce a 15-carbon accretion product (Eq. 16), closed shell species (Eq. 17) or an alkoxy radical (Eq. 18) which is not modelled explicitly but rather decomposes rapidly into another closed shell product and peroxy radical.

320

$$C10RO_2 + RO2_m \rightarrow C15d + O_2 : k_{16} \ (16)$$

$$C10RO_2 + RO2_m \rightarrow C10z/C10x/TNCARB\,26 : k_{17} \ (17)$$

325 $$C10RO_2 + RO2_m \rightarrow C10RO : k_{18} \ (18)$$
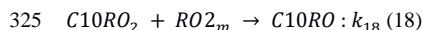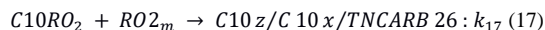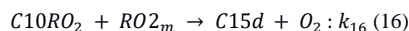
In a manner similar to C20d formation, the rate coefficient for C15d formation, k_{16}, is simulated in the mechanism to increase with the extent of oxidation of the reacting large peroxy radical. The fitting of k_{16} rate coefficients to experimental

§

data is discussed in Section 3.1.3. The chosen fitted values of $1.2\text{-}5\times10^{-12}$ cm^3 molecule^{-1} s^{-1} were lower than the range

330   measured by Berndt et al (2018b) ($1.2\text{-}3.6\times10^{-11}$ cm^3 molecule^{-1} s^{-1}).

Reaction of a large peroxy radical with the small peroxy radical pool (RO2$_s$) produces a closed shell species or an alkoxy radical, in a manner analogous to Eq. 17 and Eq. 18.

335   **2.4 HOM Loss Mechanisms**

The number of different molecules falling under the C10x, C10z, C15d and C20d umbrellas is huge, making the treatment of loss processes complex. Losses will occur via chemical or photolytic degradation as well as to condensation to aerosol, to the nucleation sink and dry and wet deposition. For simplicity, in the simulations below, we ignore wet and dry deposition but do include loss to the condensation sink for modelling simulations C and D (Table 3).

340

Chemical losses of HOMs are highly uncertain. It is suggested that HOMs will react with OH (Bianchi et al., 2019). In this model, OH reacts with C10x, C10z, C15d and C20d with the rate coefficient of the large hydroperoxide, RTN28OOH to produce the smaller closed shell CRI species CARB10 and CARB15 as well as UCARB10 (lumped methacrolein and methyl vinyl ketone) for 15-carbon dimers. Photolysis of peroxide and carbonyl linkages produce alkoxy radicals which behave as

345   previously described. Photolysis frequencies are taken from the MCM (Jenkin et al., 1997, Saunders et al., 2003). Given the small concentrations of HOMs we predict that uncertainty in these gas phase loss processes are likely to have small impacts on the general features of tropospheric chemistry (i.e. OH reactivity or ozone production).

Loss to the condensation sink presents a complex challenge. The saturation vapour pressure will vary considerably (Kurten

350   et al., 2016) for HOMs, even within the C10 umbrella, affecting the fraction which partition to the aerosol phase. Furthermore, some HOMs are likely to have aldehyde and alcohol moieties which will enhance their removal via reactive uptake into the aerosol phase, particularly if it is aqueous. When using our new mechanism in different simulations (Table 3), condensation sinks have been set to fixed values or values taken from literature.

355   Having described the additions and changes made to the base mechanism to develop our new mechanism, we now discuss the   optimisation   and   validation   of   the   mechanism.

3 Mechanism Optimisation and Validation

Here we discuss the optimisation of the new mechanism and its validation. In total 4 simulations were performed with the

360   mechanism as detailed in Table 3.

3.1 Comparison to Experimental Data

There exists a limited amount of experimental data which provides an insight into the behaviour of the multiple generations of peroxy radicals produced from ozonolysis and OH-oxidation of α-pinene (Berndt et al., 2018b). Using a flow cell, Berndt

365   measured the concentration of α-pinene-derived peroxy radicals produced by ozonolysis (O3RO2) and OH oxidation (OHRO2) and 20-carbon (C20d) and 15-carbon (C15d) accretion products at the end of the flow tube using a chemical ionisation-atmospheric pressure interface-time of flight (CI-APi-TOF) mass spectrometer and a chemical ionisation-time of

§

flight (CI3-TOF) mass spectrometer. The observed peroxy radicals spanned several generations of autoxidation, namely the 1st-4th generation for O3RO2 species and 1st-3rd generation for OHRO2. Berndt et al (2018b) also calculated rate coefficients

370   for accretion product formation using the observation that accretion product concentration increased linearly with time with an assumed uncertainty no greater than a factor of 3. Reagent ions used in the CI-APi-TOF were $C_3H_7NH_3^+$, CH_3COO^- and NO_3^- and in the CI3-TOF NH_4^+. The flow tube experiments lasted for 7.9 s, at which point the flow was sampled by the mass spectrometers. Reactions proceeded under dark conditions at 1 atm and 297 K under low $[NO_x]$ ($<10^8$ cm^{-3}). The low concentrations of bimolecular reaction partners HO_2 and NO meant that multiple autoxidation steps could occur in the

375   reaction time.

Flow tubes operating under laminar flow are easily modelled using box models as there are very few complications to consider in terms of mixing and wall loss and no new particle formation was observed. A box model version of the mechanism was compiled in the BOXMOX framework (Knote et al., 2015). The experimental data allowed the autoxidation coefficients of

380   the peroxy radical species and the rate coefficients of accretion product formation to be constrained. The concentrations of peroxy radicals and accretion products in the box model were evaluated at the end of the 7.9 s reaction period and compared with experiments. A process of iterative adjustment to autoxidation and accretion product formation rate coefficients in the mechanism was performed to produce the best reproduction of the experimental data by the mechanism.

385   Two experiments from Berndt et al (2018b) were considered. In the first experiment, flow tube runs were performed with varying initial concentrations of α-pinene (3-50 ppb) with initial O_3 at 28 ppb (Simulation A). In the second experiment, runs were performed with fixed initial α-pinene (15.6 ppb) and O_3 (80 ppb) but with initial isoprene concentrations varying from 0-60 ppb (Simulation B). Comparison to this experimental data facilitated examination of the model's ability to reproduce the concentration of HOM-precursors and accretion products with and without isoprene as well as at moderate and high O_3

390   mixing ratios.

An important parameter in the mechanism was the yield of RN26BO2 from alpha pinene ozonolysis. This yield is uncertain and it was found to affect the autoxidation coefficients required to reproduce the experimental data for the O3RO2 species. To constrain it, a first-order autoxidation rate coefficient of 0.206 s^{-1} for RN26BO2 was imposed, based on theoretical

395   analysis of the alpha pinene ozonolysis system (Kurten et al., 2015), and the yield adjusted until the mechanism was able to achieve the best possible fit to the data. This resulted in a yield of 50% for RN26BO2 and 30% for RTN24O2. However, this remains a source of uncertainty and warrants further investigation. The low NO_x conditions meant that the autoxidation coefficients dominated the concentration of later generation O3RO2 and OHRO2 and, from this starting point, the autoxidation rate coefficients for later generations were fitted against experimental data over multiple rounds of optimisation

400   (Table 4). The autoxidation coefficient for the 1st generation OHRO2, RTN28BO2, was taken as 2.1 s^{-1} based on Xu et al (2018). Estimation of the uncertainty in the autoxidation coefficient values is given in the Table S6.

The autoxidation coefficients in Table 4 are higher than those considered in the theoretical study of Scherivish et al (2019) but closer to the values measured by Zhao et al (2018) and suggested by Roldin et al (2019). The mechanism using the

405   autoxidation coefficients from Table 4 and predicted the lumped higher generation species (5th generation for O3RO2, 4th generation for OHRO2) at concentrations higher than observed in the work by Berndt et al (2018b). This suggests there may be additional, as yet unknown loss processes for the more highly oxidised peroxy radical species which are not incorporated in this work. Addition of such process would likely change the autoxidation coefficients and is an area for further study.

410   Unfortunately, the flow tube studies of Berndt et al (2018b) lack observations to constrain the full chemical space simulated

§

by the box model. In particular there were no measurements of OH, HO_2 or NO. Therefore, a rigorous series of sensitivity tests (described in the SI) were carried out to quantify the importance of uncertainty in the initial concentrations of OH, NO and HO_2 on the results of the model. Initial OH was shown to have no effect on the measured parameters (O3RO2, OHO2 and accretion products) while NO and HO_2 had some effect on OHRO2 (mainly through the change to OH) and C20d (via

415 the change to radical termination rate). Initial conditions of 10^6 cm^{-3} for OH and 4ppt for HO_2, NO and NO_2 were used. Based on the sensitivity simulations it was concluded that realistic deviations in concentration of +10 ppt / -3 ppt for HO_2, NO and NO_2 and + 10^6 cm^{-3} / -5×10^5 cm^{-3} for OH from the initial values would not lead to deviations in the concentrations of RO_2 or accretion products sufficient to warrant a change in the autoxidation coefficients.

420 **3.1.1 Varying α-pinene Experiment**

In Simulation A, the mechanism was used to simulate various experiments with increasing initial mixing ratios of α-pinene with a fixed mixing ratio of 26 ppb of O_3. The modelled 1st-4th generation O3RO2 species (Fig. 3(a)) agreed well with the observed concentrations, with all of the model results falling within experimental uncertainty bounds (although we note these are large).

425

The model was also able to reproduce the 2nd and 3rd gen OHRO2 species well (Fig. 3(a)) but struggled with the 1st generation OHRO2 species, overestimating it by a factor of 10, despite reproducing the general trend of variation with α-pinene. The experimental measurements of 1st generation OHRO2 concentration from Berndt et al (2018b) were believed to be underestimated by about a factor of 5 which explains some, but not all of the model-experimental discrepancy.

430

3.1.2 Varying Isoprene Experiment

In Simulation B, varying initial concentrations of isoprene were employed under conditions of fixed initial mixing ratios of α-pinene (15.6 ppb) and O_3 (80 ppb). The model was able to reproduce the observed decline in the 2nd and 3rd generation OHRO2 species (Fig. 4(a)) with increasing isoprene while also reproducing the minor decrease in the O3RO2 species (Fig.

435 4(b)). The decline in OHRO2 mirrored the modelled decrease in OH, providing a strong indication that OH scavenging by isoprene is playing a major role in decrease in OHRO2, as suggested by McFiggans et al (2019).

3.1.3 Simulation of Accretion Products

The 20-carbon accretion products were measured in both the isoprene-free, varying α-pinene experiment (as in Fig. 3) and,

440 separately, under conditions of constant α-pinene and varying isoprene (as in Fig. 4). As discussed in Section 2.3, the fitted rate coefficients for 20-carbon accretion product formation were varied based on the extent of oxidation of the reacting peroxy radical with the value of k_{13} ranging over 0.4-3.6 × 10^{-11} cm^3 $molecule^{-1}$ s^{-1}. This reproduced, within experimental error, the total observed C20d concentrations for both experiments (Fig. 5 and Fig. S1) and compared favourably to the values calculated by Berndt of 0.97-7.9 × 10^{-11} cm^3 $molecule^{-1}$ s^{-1}.

445

The species with the lowest functionality, the 1st generation OHRO2 (RTN28AO2 and RTN28BO2), which contain only 3 oxygens, were assigned the lowest value of k_{13} (0.4×10^{-11} cm^3 $molecule^{-1}$ s^{-1}) while the 1st generation O3RO2 (RN26BO2) with 4 oxygens were assigned k_{13}=0.97×10^{-11} cm^3 $molecule^{-1}$ s^{-1}, its self-reaction rate coefficient determined by Berndt et al (2018b). The most functionalised species for O3RO2 (RNxBOyO2) and OHRO2 (RTNxBOyO2) were assigned values of k_{13}

450 of 3.6×10^{-11} cm^3 $molecule^{-1}$ s^{-1} and 3.5×10^{-11} cm^3 $molecule^{-1}$ s^{-1} respectively. The rate coefficients used were in line with the range 0.97-7.9$ \times 10^{-11}$ cm^3 $molecule^{-1}$ s^{-1} (with an uncertainty no greater than a factor of 3) measured by Berndt et al (2018b) and the full list of values is given in the reaction list in the SI.

§

Using values of k_{13} = 0.1-3 × 10^{-12} cm^3 molecule^{-1} s^{-1}, as suggested by Roldin et al (2019) for C20d formation, produced
C20d concentrations lower than those observed (Fig S1) while values of 1-8 × 10^{-10} cm^3 molecule^{-1} s^{-1} from Molteni et al
(2019) produced values which were higher than observation.

The fitted rate coefficients for 15-carbon accretion product formation were also varied based on the extent of oxidation of the
reacting peroxy radical. Values of k_{16} ranging over 1.2 - 5 × 10^{-12} cm^3 molecule^{-1} s^{-1} (Fig. 5 and Fig. S2) reproduced observed
levels of the C15d accretion product from the constant α-pinene and variable isoprene experiments (as in Fig. 4) and were
lower than the values measured by Berndt (1.3-2.3 × 10^{-11} cm^3 molecule^{-1} s^{-1} with an uncertainty no greater than a factor of 3).

Figure 5 shows that the decrease in 20-carbon accretion products with increasing isoprene far outweighs the increase in 15-
carbon accretion products. The mechanism reproduces the general trend of suppression of total accretion product concentration
with increasing initial isoprene concentration. This finding is in good agreement with McFiggans et al (2019) and highlights a
key component of the new mechanism which simple mechanisms (e.g. Gordon et al., 2016) will miss. In the model this net
decrease in accretion products concentrations is driven in part by OH scavenging (and the subsequent reduction in OHRO2
(Fig. 4)). In this work this was the major driver of C20d decrease. However, suppression was also observed due to
scavenging of C10RO2 by isoprene-derived RO2 as observed by McFiggans et al (2019). The influence of smaller peroxy
radicals such as that from methane on accretion product formation (McFiggans et al., 2019) will be an area of future
investigation.

3.2 HOM yield variation with temperature

Autoxidation reactions have significant positive temperature dependencies (Bianchi et al., 2019, Jenkin et al., 2019a).
Accordingly, HOM yields are expected to be highly temperature sensitive. Quéléver et al (2019) recorded a 50-fold increase
in HOM yield at 293 K relative to 273 K. This temperature variation cannot be attributed to the temperature dependence of
the initial oxidation of α-pinene as the rate coefficient of ozonolysis increases only 17% between 273 K and 293 K while the
reactions with OH and NO_3 exhibit negative temperature dependencies. Frege et al (2018) measured a decrease in O:C ratio
values in HOMs with reducing temperatures, attributing this to a reduction in autoxidation.

Variation in peroxy radical structure and functionality will result in different generation peroxy radicals having different
barriers to autoxidation (Bianchi et al., 2019). A few modelling studies have considered the temperature dependencies of the
autoxidation rate coefficient in peroxy radical from α-pinene derivatives. Schervish et al (2019) considered a simple
approach where all generations of peroxy radicals from α-pinene ozonolysis had a fixed activation energy of 62.4 or 66.5 KJ
mol^{-1} (θ = 7500-8000 K when rate coefficient is expressed as k=Ae$^{-\theta/T}$), while noting that a reduction in barriers to
autoxidation with increasing functionality is plausible but so far unproven. By contrast, Roldin et al (2019) considered a
higher activation energy of 100.4 KJ mol^{-1} (θ = 12077 K) based on the theoretical work of Kurtén et al (2015) which
identified activation energies of 90-120 KJ mol^{-1} for α-pinene.

Given the lack of additional literature in this area, 4 versions of the new mechanism were created to probe the effects of
temperature and activation energy on HOM yield and subsequent evolution. In each mechanism all autoxidation reactions
(for O3RO2 and OHRO2) had the same activation energy while all other rate coefficients were the same across mechanisms
(Table S2). Activation barriers of θ = 6000 K, θ = 9000 K and θ = 12077 K were chosen as they included the range
suggested by Roldin et al (2019) and Schervish et al (2019) and the mechanism versions termed HOM$_{6000}$, HOM$_{9000}$ and

§

495   HOM_{12077} respectively. For the temperature dependent versions, the pre-exponential factor of the autoxidation coefficient (Table S5) was adjusted so that the autoxidation coefficients were the same at 297 K as those derived from the comparison to experimental data from Berndt et al (2018b). It is recognised that the autoxidation steps are likely to have different activation energies, but this analysis provides a first approximation of the influence of activation energy on HOM formation.

500   In a simulation modelling an instantaneous injection of α-pinene (Simulation C), the HOM yield for the 10-carbon species, individually and in total (defined in the SI), was calculated with the three different temperature dependencies (HOM_{6000}, HOM_{9000} and HOM_{12077}) at temperatures of 270 K, 290 K and 310 K for initials conditions of α-pinene 15 ppb, O_3 40 ppb and OH at 10^6 cm^{-3} and a temperature independent condensation sink of 2×10^{-3} s^{-1}.

505   Figure 6(a) shows the results from the simulations performed with initial concentrations of NO and NO_2 of 0.01-10 ppb. These simulations showed that the 10-carbon HOM yield tends to increase slightly from very low (0.01 ppb) to moderate (1 ppb) NO_x and then decline rapidly with increasing NO_x thereafter. This behaviour is likely to be due to the inclusion in the mechanism of the isomerisation pathway via reaction with NO which yields the next generation peroxy radical. This pathway has been suggested as an important route for forming more highly oxidised derivatives of alpha pinene due to the 510   potential rapid ring-opening mechanism involving alkoxy radicals and the cyclobutyl ring found in alpha pinene ozonolysis products (Rissanen et al., 2015). Figure 6(a) indicates that the absolute yield is also sensitive to temperature, with the highest yields simulated at the highest temperatures. At low temperatures (blue data), the uncertainty in autoxidation temperature dependence has the greatest effect while at high temperature this feature is muted. The increase in yield with temperature is in qualitative agreement with observation (Quéléver et al., 2019, Simon et al., 2019).

515

The model predicted total HOM yields at 290 K of 4.5±0.4 % (0.01 ppb NO) to 5.7±0.4% (1 ppb NO), well within the ranges previously suggested by Ehn et al (2014) (3.5-10.5 %) at similar temperature and α-pinene concentrations as well as comparing favourably to yield measured by Sarnela et al (2018) (3.5-6.5%), Jokinen et al (2014) (1.7-6.8 %) and Roldin et al (2019) (7%) indicating that the mechanism is doing a good job at simulating HOM yield. In addition, the HOM yield at 270 520   K of ~0.7-3 % compared favourably with the yield of ~2% determined by Roldin et al (2019).

3.3 Comparison to CRI v2.2

The ability of the new mechanism to reproduce the concentrations of key atmospheric species from the CRI v2.2 under different emissions of NO_x and α-pinene was assessed using an 8 day box modelling run (Simulation D). Over the majority 525   of emissions space, O_3 differed by less than 0.05 ppb (0.1%), OH by less than 0.4% and NO by less than 2.5 ppt (0.4%) (Fig. S4-S6) with similar (or better) agreement for other important species (Fig. S7-S15). Acetone was routinely underpredicted (Fig. S16) by between a factor of ~14 at 50 ppt NO_x and by ~20 % at 2-10 ppb of NO_x but this did not result in significant deviation between the base mechanism and new mechanism for O_3 or OH. This indicates that the basic features of atmospheric chemistry, such as HO_x recycling processes added in the CRI v2.2, which have been shown to have important 530   consequences for atmospheric composition (Jenkin et al., 2019b), are preserved in the new mechanism.

3.3.1 Peroxy Radicals and HOMs

§

As our model simulations indicate, and as has previously been observed (Lehtipalo et al., 2018), at higher concentrations of
NO$_x$ there is inhibition of HOM formation with the principle driver being the reaction of NO with peroxy radicals occurring
at a rate outcompeting autoxidation. While reaction with NO can in part aid HOM formation by increasing the isomerisation
pathway, the fragmentation pathway (forming smaller species) and formation of non-HOM nitrates leads to a reduction in
total HOM. Accordingly, all these mechanisms predict a decrease in HOM concentration with increasing NO$_x$ (Fig. 6(b)).
Furthermore, very little difference is observed between the different HOM mechanisms, suggesting that uncertainty in the
activation energy may not be too great an impediment to understanding general HOM behaviour, at least at the temperatures
considered.

However, it should be remembered that, at present, the HOM tracers in the mechanism represent a range of species with
varying levels of oxidation. For example, C10z corresponds to HOMs formed from 2nd to 5th O3RO2 generations of O3RO2
and C10x to HOMs from all generations of OHRO2. The predicted concentrations of different generations of O3RO2 (Fig.
S17) and OHRO2 (Fig. S18) were also observed to decrease with NO$_x$ with little difference between different HOM
mechanisms. Furthermore, the most abundant peroxy radicals for both pathways were the lumped highest generation species,
highlighting the potential issue of lack of loss processes for the most highly oxidised RO$_2$ species as was encountered when
fitting parameters to flow cell data.

3.3.2 Closed Shell and non-HOM Species

In the base mechanism, α-pinene oxidation predominantly leads to the formation of the closed shell species CARB16 and
TNCARB26 (carbonyls) and RN18NO3 and RTN28NO3 (nitrates). Whilst the base mechanism has been optimised against
the MCM, these pathways have not themselves been tuned extensively to reproduce concentrations observed in experimental
systems. These species are still present in the new mechanism but the concentrations of RTN28NO3 and TNCARB26 are
predicted to be slightly lower than in the base mechanism (Fig. S19) while CARB16 is simulated as being much lower in
concentration than in the base mechanism at low NO$_x$ with the difference attributed to the added competition from the
autoxidation pathways.

The nitrate species formed from RN18AO2 in the base mechanism, RN18NO3, is significantly lower in the HOM
mechanism. Nitrate yield is a complicated topic, not least because the MCM predicts that the peroxy radicals C107O2 and
C109O2, which are used to represent the 1st generation O3RO2 in part (RN26BO2), do not form nitrate upon reaction with
NO or NO$_3$. Importantly this does not affect the O$_3$ and OH concentrations, but this should be an area that future work
addresses.

4 Simulation of HOM Vertical Profiles

Given the success of the mechanism in simulating the laboratory flow tube experiments and its ability to capture the
sensitivity of HOMs to changes in the reactivity of the peroxy radical pool, we focus now on using the scheme to simulate
tropospheric conditions to investigate, to first order, how the scheme would predict ambient HOM concentrations. Here we
focus on using our new mechanism to simulate the surface [HOMs] and the vertical profile of [HOMs]. We also at the effect
of the simulated HOMs on nucleation rates in the lower troposphere.

The vertical profiles of HOMs over the boreal forest near Hyttalia in Finland (61° 9' N, 23° 4' E) and near Manaus in the
Amazon rainforest (-2° 35' N, 60° 12' W) were investigated along with surface concentrations representative of Brent,

§

Alabama (32.903°N, 87.250°W). For each altitude level, the sensitivity simulations were performed with three different activation energies for the autoxidation steps (HOM_{6000}, HOM_{9000} and HOM_{12077}). Vertical transport was neglected - a different box model was run at each vertical level with the inputs being the output of a simulation with the UKCA model (Archibald et al., 2019) sampled at 14:00 LT (photolysis frequencies were adjusted to account for the solar zenith angle but

580 not for altitude variation). Hourly concentration data from UKCA were provided for O_3, OH, isoprene, α-pinene, HO_2, NO, NO_2, NO_3, N_2O_5, temperature and pressure for 16th June averaged over 2010-2014, from the grid boxes in UKCA corresponding to the respective locations discussed above, and supplemented with monthly mean concentrations of a further 23 species (Table S3) with the concentration of certain species adjusted to observations (Kuhn et al., 2007 and Table 4.1) and scaled vertically to account for biases in the UKCA output. HOM condensations sinks (CS) (equal for all HOM species)

585 discussed in Lee et al (2016) (Table S4) were used at the surface and scaled using the modelled vertical profile of aerosol surface area density. Sensitivity studies revealed that the output of the 1D box modelling shows significant sensitivity of [HOMs] to the magnitude and profile of the CS (Fig. S20). Therefore, we can suggest that our simulated vertical profiles be regarded as semi-qualitative as more work is required to identify if the condensation sink should be species dependent.

590 Table 5 summarises the comparison of our model simulations of near surface [HOMs] compared to observations. In the boreal forest in Hyytiala, the range of predicted 10-carbon [HOM] is close to the mean observational value (Roldin et al., 2019) and the predicted 20-carbon accretion product concentration is slightly above the observational range. In Alabama, the model produces a reasonable value given that the observation dataset includes 9-carbon species not considered in the model at present. The model results in Table 5 provide strong support that when implemented in a global chemistry climate model,

595 our new scheme should perform well if the underlying emissions of BVOCs and NO_x and the CS are well simulated.

Figure 7 shows the concentrations of the different HOMs from the box model version as a function of altitude above Hyytiala and over the Amazon rainforest near Manaus. In both locations, the 10-carbon HOM profiles roughly mirror alpha-pinene with roughly equal abundance of the species from ozonolysis and OH oxidation. In spite of higher [BVOCs], the

600 considerably higher CS in the Amazon region (Lee et al., 2016) resulted in lower [HOM] within the boundary layer than at Hyytiala, while the warmer temperatures also resulted in a negligible dependence on the activation energy in the lowest 4 km (i.e. the shaded areas are smaller in Fig. 7(b) than in Fig. 7(a)).

Hyytiala and the Amazon represent very different chemical environments with the isoprene/α-pinene ratio (I/AP) playing an

605 important role in the accretion product distribution; 15-carbon accretion products are simulated as being more abundant than 20-carbon accretion products in the Amazon with the biggest difference predicted at low altitude where I/AP is greatest. By contrast, in Hyytiala where I/AP is smaller, 20-carbon accretion products are more abundant.

Figure 7 highlights strong vertical profiles for the simulated [HOMs]. The simulations over the Amazon suggest a significant

610 secondary peak in [HOMs] at around 4-5 km in altitude; in part linked to an increase in the [BVOCs] at this height. In our simulations each vertical level is represented by a different box model simulation so there is no simulation of the advection of HOMs. It will be interesting to see how future fully coupled model simulations simulate the vertical profile of [HOMs] and how this affects processes like aerosol formation and climate.

§

4.1 Nucleation Rates

615

Given the important role Gordon et al (2016) identified for HOMs in NPF we extend our 1-D calculations to investigate the implications of the predicted HOM profiles on nucleation rates using monthly mean climate model data from the PD and PI. Nucleation rates from two different nucleation mechanisms were studied: (i) neutral and ion-induced pure biogenic nucleation (PBN) (Kirkby et al., 2016); and (ii) activation of sulphuric acid (SA_{act}) (Kulmala et al., 2006; Sihto et al., 2006) suitable for the boundary layer. The results of the calculations of nucleation rates using these schemes are summarised in Figure 8. (The nucleation rate expressions are given in the SI.)

There exists little observational data on nucleation solely from PBN mechanisms, making model validation hard. Modelled surface sulphuric acid concentrations at Hyytiala ($2\text{-}3\times10^6$ cm^{-3}) fall within the range of observations ($3\times10^5\text{-}2\times10^7$ cm^{-3} (Boy et al., 2005, Petäjä et al., 2009)). Modelled concentrations in the Amazon (3×10^4 cm^{-3}) were slightly lower than observation ($10^5\text{-}10^6$ cm^{-3} (Wimmer et al., 2018)) although the observations were taken in a pasture site downwind of Manaus surrounded by the rainforest not in the rainforest itself and are therefore likely to be higher than in-situ rainforest values. Thus, the nucleation rates we have calculated for SA_{act} are likely to be a reasonable estimate in Hyytiala and slightly low biased in the Amazon.

Figure 8 shows predicted nucleation rates in the PI and PD in the Amazon and Hyytiala derived from our simulated [HOMs] vertical profile in the boundary layer and low free troposphere using June monthly mean data from a UKESM historical run taken from the PI (June average 1851-1856) and PD (June average 2009-2014). In all cases, the PBN nucleation rates decline rapidly with height above the boundary layer. In the Boreal forest, the nucleation rate from PBN at very low altitudes is calculated to be around 20-25% of that from SA_{act} in the PD. However, in the PI it is comparable to the SA_{act} rate, contributing 40-80 % of the total nucleation rate in the lowest 500 m (Fig. S21). The greater relative importance of PBN in the PI, despite lower predicted [HOM], was attributed to two factors. Firstly, predicted steady state ion concentrations were higher in the PI in Finland than the PD due to the PI's lower ion CS. This increased the rate of the ion-induced pathway PBN pathway. Secondly, the considerably lower modelled concentrations of sulphuric acid in PI (around 10x lower than in the PD) reduced the importance of SA_{act}. By contrast, the lower concentrations of predicted [HOM] in the Amazon led to PBN having a much smaller contribution to the total nucleation rate (< 5% in the PD and a negligible impact in the PI). This is in agreement with multiple sources (Andreae et al., 2015, Wimmer et al., 2018, Rizzo et al., 2018). The importance of PBN in the PI atmosphere in certain locations, qualitatively in agreement with Gordon et al (2016), illustrates the potential importance including PBN in climate models could have on aerosol burden and the associated radiative effects.

5 Summary and Conclusions

We present a novel chemical mechanism, CRI-HOM, for simulating HOM formation based on the latest version of the Common Representative Intermediate scheme (CRI v2.2). Focusing on the most important natural source of HOMs, α-pinene, the CRI-HOM mechanism is one of the first HOM mechanisms ready for incorporation into existing chemistry-aerosol climate models. The scheme is much more complex than previous steady state approximations (Gordon et al., 2016) and so enables non-linear interactions and feedbacks with the chemical environment to be represented, but far more concise than other mechanisms that have been developed which treat the complex structural characteristics of the formation of HOMs (Roldin et al., 2019). The addition of 12 new species and 66 reactions means that this scheme can be used for long term global chemistry-aerosol-climate studies.

§

Firstly, the mechanism was optimised against flow cell data and validated by comparison to observed HOM yields. A key result was the ability of the mechanism to reproduce observations of isoprene driving a decline in HOM peroxy radical precursors and 20-carbon accretion products (and total accretion product concentration) (McFiggans et al., 2019). The need for further research into the loss processes of the highly oxidised peroxy radicals was identified to reconcile the disparity

660   between modelled and observed concentrations. The effect of other peroxy radicals, such as those from smaller more abundant organic species, on accretion product formation is also an area for future investigation.

After optimisation, the CRI-HOM was compared to the base mechanism (CRI v2.2) and very good agreement was observed for a wide range of atmospheric gases including O_3, OH and its precursors. This indicated that the important features of HO_x

665   recycling and accurate O_3 representation, developed in the CRI v2.2, had been preserved in CRI-HOM.

In further tests of CRI-HOM, HOM yields and concentrations were predicted to decrease with increasing NO_x and increase with temperature, in agreement with previous theoretical and observational studies. The temperature dependence of autoxidation was investigated using activation energies spanning the range of values suggested in literature (Roldin et al.,

670   2019, Schervish et al., 2019). Temperature dependence was predicted to have a significant effect on HOM yield at 270 K but a much smaller effect at 290 K and 310 K.

In a final experiment, vertical profiles of HOM were simulated using a pseudo 1D box model for Finland, Alabama and the Amazon using chemistry climate model data as inputs. The model performed well relative to observations in Finland and

675   Alabama. The influence of the condensation sink (CS) value on [HOM] was shown to be significant with [HOM] predicted to be significantly lower in the Amazon, despite higher [BVOC], due to the higher CS. Improving the description of the CS within the mechanism has been identified as an important area of future work. The profiles also illustrated the dependence of HOM on the chemical environment, driven chiefly by the interaction of isoprene and monoterpenes. The higher concentrations of isoprene in the Amazon resulted in lower concentrations of the most involatile species, the 20-carbon

680   accretion product. Simulated [HOM] were also used to probe the importance of various particle nucleation mechanisms. In Finland, pure biogenic nucleation mechanism (i.e. nucleation without sulphuric acid) at low altitude was predicted to be responsible for around 60% of new particle formation in the lowest 500 m in the pre-industrial atmosphere and around 20% in the present day, indicating the importance of HOMs, particularly in the pre-industrial, with implications for aerosol burden and climate. PBN was predicted to be less important in the Amazon given the lower simulated [HOM].

685

CRI-HOM can provide a framework for simulating HOMs in global chemistry-aerosol-climate studies and simulating the effects of isoprene-driven suppression of involatile biogenic-derived species and the consequences on SOA and NPF while also providing a state-of-the-art description of atmospheric chemistry. Such an effect, and the influence on the proposed "BVOC negative feedback", is likely to be important in a warming climate with enhanced emissions of BVOCs and

690   determining the size and sign of the feedback. Once incorporated into a global chemistry-aerosol-climate model, assessing the effect of HOMs on pre-industrial, present day and future climate will be key area of future work.

Supplement. The supplement related to the article is available online.

§

700

Data Availability. All modelled data is available upon request from James Weber and all experimental data from Torsten Berndt.

Author Contributions. Mechanism development was done by JW, ATA, ME, SA, modelling experiments were designed and
705 executed by JW, ATA, PG, HG, CK and flow cell data was compiled and interpreted by TB. JW and ATA wrote the paper. All co-authors discussed the results and commented on the paper.

Competing Interests. All authors declare that they have no competing interests.

References

710 Andreae, M. O., Acevedo, O. C., Araùjo, A., Artaxo, P., Barbosa, C. G. G., Barbosa, H. M. J., Brito, J., Carbone, S., Chi, X., Cintra, B. B. L., da Silva, N. F., Dias, N. L., Dias-Júnior, C. Q., Ditas, F., Ditz, R., Godoi, A. F. L., Godoi, R. H. M., Heimann, M., Hoffmann, T., Kesselmeier, J., Könemann, T., Krüger, M. L., Lavric, J. V., Manzi, A. O., Lopes, A. P., Martins, D. L., Mikhailov, E. F., Moran-Zuloaga, D., Nelson, B. W., Nölscher, A. C., Santos Nogueira, D., Piedade, M. T. F., Pöhlker, C., Pöschl, U., Quesada, C. A., Rizzo, L. V., Ro, C.-U., Ruckteschler, N., Sá, L. D. A., de Oliveira Sá, M., Sales,
715 C. B., dos Santos, R. M. N., Saturno, J., Schöngart, J., Sörgel, M., de Souza, C. M., de Souza, R. A. F., Su, H., Targhetta, N., Tóta, J., Trebs, I., Trumbore, S., van Eijck, A., Walter, D., Wang, Z., Weber, B., Williams, J., Winderlich, J., Wittmann, F., Wolff, S., and Yáñez-Serrano, A. M.: The Amazon Tall Tower Observatory (ATTO): overview of pilot measurements on ecosystem ecology, meteorology, trace gases, and aerosols,

720 Archibald, A.T., Abraham, N.L., Bellouin, N., Boucher, O., Braesicke, P., Bushell, A., Carslaw, K., Collins, B., Dalvi, M., Emmerson, K. and Folberth, G., 2019. Unified Model Documentation Paper No. 84: United Kingdom Chemistry and Aerosol (UKCA) Technical Description MetUM Version 11.3. UK Met Office, Exeter, UK.

Bates, K. H. and Jacob, D. J.: A new model mechanism for atmospheric oxidation of isoprene: global effects on oxidants,
725 nitrogen oxides, organic products, and secondary organic aerosol, Atmos. Chem. Phys., 19, 9613–9640, doi.org/10.5194/acp-19-9613-2019, 2019.

Berndt, T., Scholz, W., Mentler, B., Fischer, L., Herrmann, H., Kulmala, M. and Hansel, A.: Accretion Product Formation from Self-and Cross-Reactions of RO2 Radicals in the Atmosphere. Angewandte Chemie International Edition, 57, 3820-
730 3824, doi.org/10.1002/anie.201710989, 2018a.

Berndt, T., Mentler, B., Scholz, W., Fischer, L., Herrmann, H., Kulmala, M. and Hansel, A.: Accretion product formation from ozonolysis and OH radical reaction of α-pinene: mechanistic insight and the influence of isoprene and ethylene. Environmental science & technology, 52,11069-11077, doi.org/10.1021/acs.est.8b02210, 2018b.
735

Bianchi, F., Kurtén, T., Riva, M., Mohr, C., Rissanen, M.P., Roldin, P., Berndt, T., Crounse, J.D., Wennberg, P.O., Mentel, T.F. and Wildt, J.: Highly oxygenated organic molecules (HOM) from gas-phase autoxidation involving peroxy radicals: A key contributor to atmospheric aerosol. Chemical reviews, 119, 3472-3509, doi.org/10.1021/acs.chemrev.8b00395, 2019.

740 Boy, M., Kulmala, M., Ruuskanen, T. M., Pihlatie, M., Reissell, A., Aalto, P. P., Keronen, P., Dal Maso, M., Hellen, H., Hakola, H., Jansson, R., Hanke, M., and Arnold, F.: Sulphuric acid closure and contribution to nucleation mode particle growth, Atmos. Chem. Phys., 5, 863–878, doi.org/10.5194/acp-5-863-2005, 2005.

§

Carslaw, K. S., Boucher, O., Spracklen, D. V., Mann, G. W., Rae, J. G. L., Woodward, S., and Kulmala, M.: A review of

745   natural aerosol interactions and feedbacks within the Earth system, Atmos. Chem. Phys., 10, 1701-1737, doi.org/10.5194/acp-10-1701-2010, 2010

Crounse, J.D., Nielsen, L.B., Jørgensen, S., Kjaergaard, H.G. and Wennberg, P.O.: Autoxidation of organic compounds in the atmosphere. The Journal of Physical Chemistry Letters, 4), 3513-3520, doi.org/10.1021/jz4019207, 2013.

750

Ehn, M., Kleist, E., Junninen, H., Petäjä, T., Lönn, G., Schobesberger, S., Maso, M.D., Trimborn, A., Kulmala, M., Worsnop, D.R. and Wahner, A.: Gas phase formation of extremely oxidized pinene reaction products in chamber and ambient air. Atmospheric chemistry and physics, 12, 5113-5127, doi:10.5194/acpd-12-4589-2012, 2012.

755   Jokinen, T., Berndt, T., Makkonen, R., Kerminen, V.M., Junninen, H., Paasonen, P., Stratmann, F., Herrmann, H., Guenther, A.B., Worsnop, D.R. and Kulmala, M.: Production of extremely low volatile organic compounds from biogenic emissions: Measured yields and atmospheric implications. Proceedings of the National Academy of Sciences, 112, 7123-7128, doi.org/10.1073/pnas.1423977112, 2014.

760   Frege, C., Ortega, I. K., Rissanen, M. P., Praplan, A. P., Steiner, G., Heinritzi, M., Ahonen, L., Amorim, A., Bernhammer, A.-K., Bianchi, F., Brilke, S., Breitenlechner, M., Dada, L., Dias, A., Duplissy, J., Ehrhart, S., El-Haddad, I., Fischer, L., Fuchs, C., Garmash, O., Gonin, M., Hansel, A., Hoyle, C. R., Jokinen, T., Junninen, H., Kirkby, J., Kürten, A., Lehtipalo, K., Leiminger, M., Mauldin, R. L., Molteni, U., Nichman, L., Petäjä, T., Sarnela, N., Schobesberger, S., Simon, M., Sipilä, M., Stolzenburg, D., Tomé, A., Vogel, A. L., Wagner, A. C., Wagner, R., Xiao, M., Yan, C., Ye, P., Curtius, J., Donahue, N. M.,

765   Flagan, R. C., Kulmala, M., Worsnop, D. R., Winkler, P. M., Dommen, J., and Baltensperger, U.: Influence of temperature on the molecular composition of ions and charged clusters during pure biogenic nucleation, Atmos. Chem. Phys., 18, 65–79, doi.org/10.5194/acp-18-65-2018, 2018.

Gordon, H., Kirkby, J., Baltensperger, U., Bianchi, F., Breitenlechner, M., Curtius, J., Dias, A., Dommen, J., Donahue,

770   N.M., Dunne, E.M. and Duplissy, J.: Causes and importance of new particle formation in the present-day and preindustrial atmospheres. Journal of Geophysical Research: Atmospheres, 122, 8739-8760, doi.org/10.1002/2017JD026844, 2017.

Hirsikko, A., Nieminen, T., Gagné, S., Lehtipalo, K., Manninen, H. E., Ehn, M., Hõrrak, U., Kerminen, V.-M., Laakso, L., McMurry, P. H., Mirme, A., Mirme, S., Petäjä, T., Tammet, H., Vakkari, V., Vana, M., and Kulmala, M.: Atmospheric ions

775   and nucleation: a review of observations, Atmos. Chem. Phys., 11, 767–798, doi.org/10.5194/acp-11-767-2011, 2011.

Jenkin, M.E., Saunders, S.M. and Pilling, M.J.: The tropospheric degradation of volatile organic compounds: a protocol for mechanism development. Atmospheric Environment, 31, 81-104, doi.org/10.1016/S1352-2310(96)00105-7, 1997.

780   Jenkin, M.E., Watson, L.A., Utembe, S.R. and Shallcross, D.E.:. A Common Representative Intermediates (CRI) mechanism for VOC degradation. Part 1: Gas phase mechanism development. Atmospheric Environment, 42,.7185-7195, doi.org/10.1016/j.atmosenv.2008.07.028, 2008.

Jenkin, M. E., Young, J. C., and Rickard, A. R.: The MCM v3.3.1 degradation scheme for isoprene, Atmos. Chem. Phys.,

785   15, 11433–11459, doi.org/10.5194/acp-15-11433-2015, 2015.

Atmospheric
Chemistry
and Physics
Discussions

§

Jenkin, M. E., Valorso, R., Aumont, B., and Rickard, A. R.: Estimation of rate coefficients and branching ratios for reactions of organic peroxy radicals for use in automated mechanism construction, Atmos. Chem. Phys., 19, 7691–7717, doi.org/10.5194/acp-19-7691-2019, 2019a.

790

Jenkin, M.E., Khan, M.A.H., Shallcross, D.E., Bergström, R., Simpson, D., Murphy, K.L.C. and Rickard, A.R.: The CRI v2. 2 reduced degradation scheme for isoprene. Atmospheric Environment, 212, 172-182, doi.org/10.1016/j.atmosenv.2019.05.055, 2019b.

795 Jokinen, T., Sipilä, M., Richters, S., Kerminen, V.M., Paasonen, P., Stratmann, F., Worsnop, D., Kulmala, M., Ehn, M., Herrmann, H. and Berndt, T.: Rapid autoxidation forms highly oxidized RO_2 radicals in the atmosphere. Angewandte Chemie International Edition, 53, 14596-14600, https://doi.org/10.1002/anie.201408566, 2014.

Kiendler-Scharr, A., Wildt, J., Dal Maso, M., Hohaus, T., Kleist, E., Mentel, T.F., Tillmann, R., Uerlings, R., Schurr, U. and
800 Wahner, A.: New particle formation in forests inhibited by isoprene emissions. Nature, 461, 381-384,doi.org/10.1038/nature08292   2009.   .

Kirkby, J., Duplissy, J., Sengupta, K., Frege, C., Gordon, H., Williamson, C., Heinritzi, M., Simon, M., Yan, C., Almeida, J. and Tröstl, J.: Ion-induced nucleation of pure biogenic particles. Nature, 533, 521–526, doi.org/10.1038/nature17953, 2016..

805

Knote, C., Tuccella, P., Curci, G., Emmons, L., Orlando, J.J., Madronich, S., Baró, R., Jiménez-Guerrero, P., Luecken, D., Hogrefe, C. and Forkel, R.: Influence of the choice of gas-phase mechanism on predictions of key gaseous pollutants during the AQMEII phase-2 intercomparison. Atmospheric Environment, 115, 553-568, /doi.org/10.1016/j.atmosenv.2014.11.066, 2015.

810

Kuhn, U., Andreae, M. O., Ammann, C., Araújo, A. C., Brancaleoni, E., Ciccioli, P., Dindorf, T., Frattoni, M., Gatti, L. V., Ganzeveld, L., Kruijt, B., Lelieveld, J., Lloyd, J., Meixner, F. X., Nobre, A. D., Pöschl, U., Spirig, C., Stefani, P., Thielmann, A., Valentini, R., and Kesselmeier, J.: Isoprene and monoterpene fluxes from Central Amazonian rainforest inferred from tower-based and airborne measurements, and implications on the atmospheric chemistry and the local carbon
815 budget, Atmos. Chem. Phys., 7, 2855–2879, doi.org/10.5194/acp-7-2855-2007, 2007.

Kulmala, M., Laaksonen, A. and Pirjola, L.: Parameterizations for sulfuric acid/water nucleation rates. Journal of Geophysical Research: Atmospheres, 103, 8301-8307, doi.org/10.1029/97JD03718, 1998.

820 Kulmala, M., Lehtinen, K. E. J., and Laaksonen, A.: Cluster activation theory as an explanation of the linear dependence between formation rate of 3nm particles and sulphuric acid concentration, Atmos. Chem. Phys., 6, 787–793, doi.org/10.5194/acp-6-787-2006, 2006.

Kulmala M., Nieminen T., Chellapermal R., Makkonen R., Bäck J., Kerminen VM.: Climate Feedbacks Linking the
825 Increasing Atmospheric CO_2 Concentration, BVOC Emissions, Aerosols and Clouds in Forest Ecosystems. In: Niinemets Ü., Monson R. (eds) Biology, Controls and Models of Tree Volatile Organic Compound Emissions. Tree Physiology, vol 5. Springer, Dordrecht, doi.org/10.1007/978-94-007-6606-8_17, 2013.

§

Kurtén, T., Rissanen, M.P., Mackeprang, K., Thornton, J.A., Hyttinen, N., Jørgensen, S., Ehn, M. and Kjaergaard, H.G.:
830   Computational study of hydrogen shifts and ring-opening mechanisms in α-pinene ozonolysis products. The Journal of
Physical Chemistry A, 119, 11366-11375, doi.org/10.1021/acs.jpca.5b08948, 2015.

Lee, S.H., Uin, J., Guenther, A.B., de Gouw, J.A., Yu, F., Nadykto, A.B., Herb, J., Ng, N.L., Koss, A., Brune, W.H. and
Baumann, K.: Isoprene suppression of new particle formation: Potential mechanisms and implications. Journal of
835   Geophysical Research: Atmospheres, 121,14-621, doi.org/10.1002/2016JD024844, 2016.

Lehtipalo, K., Yan, C., Dada, L., Bianchi, F., Xiao, M., Wagner, R., Stolzenburg, D., Ahonen, L.R., Amorim, A., Baccarini,
A. and Bauer, P.S.: Multicomponent new particle formation from sulphuric acid, ammonia, and biogenic vapors. Science
advances, 4, p.eaau5363, 10.1126/sciadv.aau5363, 2018.

840

McFiggans, G., Mentel, T.F., Wildt, J., Pullinen, I., Kang, S., Kleist, E., Schmitt, S., Springer, M., Tillmann, R., Wu, C. and
Zhao, D.: Secondary organic aerosol reduced by mixture of atmospheric vapours. Nature, 565, 587-593,
doi.org/10.1038/s41586-018-0871-y, 2019.

845   Molteni, U., Simon, M., Heinritzi, M., Hoyle, C.R., Bernhammer, A.K., Bianchi, F., Breitenlechner, M., Brilke, S., Dias, A.,
Duplissy, J. and Frege, C.:. Formation of Highly Oxygenated Organic Molecules from α-Pinene Ozonolysis: Chemical
Characteristics, Mechanism, and Kinetic Model Development. ACS Earth and Space Chemistry, 3, 873-
883,doi.org/10.1021/acsearthspacechem.9b00035, 2019.

850   Petäjä, T., Mauldin, III, R. L., Kosciuch, E., McGrath, J., Nieminen, T., Paasonen, P., Boy, M., Adamov, A., Kotiaho, T.,
and Kulmala, M.: Sulphuric acid and OH concentrations in a boreal forest site, Atmos. Chem. Phys., 9, 7435–7448,
doi.org/10.5194/acp-9-7435-2009, 2009.

Quéléver, L. L. J., Kristensen, K., Normann Jensen, L., Rosati, B., Teiwes, R., Daellenbach, K. R., Peräkylä, O., Roldin, P.,
855   Bossi, R., Pedersen, H. B., Glasius, M., Bilde, M., and Ehn, M.: Effect of temperature on the formation of highly oxygenated
organic molecules (HOMs) from alpha-pinene ozonolysis, Atmos. Chem. Phys., 19, 7609–7625, doi.org/10.5194/acp-19-
7609-2019, 2019.

Riccobono, F., Schobesberger, S., Scott, C.E., Dommen, J., Ortega, I.K., Rondo, L., Almeida, J., Amorim, A., Bianchi, F.,
860   Breitenlechner, M. and David, A.: Oxidation products of biogenic emissions contribute to nucleation of atmospheric
particles. Science, 344, 717-721, doi:10.1126/science.1243527 , 2014.

Varanda Rizzo, L., Roldin, P., Brito, J., Backman, J., Swietlicki, E., Krejci, R., Tunved, P., Petäjä, T., Kulmala, M. and
Artaxo, P.: Multi-year statistical and modeling analysis of submicrometer aerosol number size distributions at a rain forest
865   site in Amazonia. Atmospheric Chemistry and Physics, 18,10255-10274, /doi.org/10.5194/acp-18-10255-2018, 2018.

Roldin, P., Ehn, M., Kurtén, T., Olenius, T., Rissanen, M.P., Sarnela, N., Elm, J., Rantala, P., Hao, L., Hyttinen, N. and
Heikkinen, L..: The role of highly oxygenated organic molecules in the Boreal aerosol-cloud-climate system. Nature
communications, 10, 1-15, doi.org/10.1038/s41467-019-12338-8, 2019.

870

§

Sarnela, N., Jokinen, T., Duplissy, J., Yan, C., Nieminen, T., Ehn, M., Schobesberger, S., Heinritzi, M., Ehrhart, S., Lehtipalo, K., Tröstl, J., Simon, M., Kürten, A., Leiminger, M., Lawler, M. J., Rissanen, M. P., Bianchi, F., Praplan, A. P., Hakala, J., Amorim, A., Gonin, M., Hansel, A., Kirkby, J., Dommen, J., Curtius, J., Smith, J. N., Petäjä, T., Worsnop, D. R., Kulmala, M., Donahue, N. M., and Sipilä, M.: Measurement–model comparison of stabilized Criegee intermediate and
875   highly oxygenated molecule production in the CLOUD chamber, Atmos. Chem. Phys., 18, 2363–2380, doi.org/10.5194/acp-18-2363-2018, 2018.

Saunders, S. M., Jenkin, M. E., Derwent, R. G., and Pilling, M. J.: Protocol for the development of the Master Chemical Mechanism, MCM v3 (Part A): tropospheric degradation of non-aromatic volatile organic compounds, Atmos. Chem. Phys.,
880   3, 161–180, doi.org/10.5194/acp-3-161-2003, 2003.

Schervish, M. and Donahue, N. M.: Peroxy Radical Chemistry and the Volatility Basis Set, Atmos. Chem. Phys. Discuss., doi.org/10.5194/acp-2019-509, in review, 2019.

885   Shrivastava, M., Cappa, C.D., Fan, J., Goldstein, A.H., Guenther, A.B., Jimenez, J.L., Kuang, C., Laskin, A., Martin, S.T., Ng, N.L. and Petaja, T., 2017. Recent advances in understanding secondary organic aerosol: Implications for global climate forcing. Reviews of Geophysics, 55, 509-559, doi.org/10.1002/2016RG000540, 2017.

Sihto, S.-L., Kulmala, M., Kerminen, V.-M., Dal Maso, M., Petäjä, T., Riipinen, I., Korhonen, H., Arnold, F., Janson, R.,
890   Boy, M., Laaksonen, A., and Lehtinen, K. E. J.: Atmospheric sulphuric acid and aerosol formation: implications from atmospheric mea- surements for nucleation and early growth mechanisms, Atmos. Chem. Phys., 6, 4079–4091, doi:10.5194/acp-6-4079-2006, 2006

Sporre, M.K., Blichner, S.M., Karset, I.H., Makkonen, R. and Berntsen, T.K.. BVOC–aerosol–climate feedbacks
895   investigated using NorESM. Atmospheric Chemistry and Physics, 19, 4763-4782, doi.org/10.5194/acp-19-4763-2019, 2019.

Stocker, T. F., Qin, D., Plattner, G.-K., Alexander, L. V., Allen, S. K., Bindoff, N. L., Br\'on, F.-M., Church, J. A., Cubasch, U., Emori, S., Forster, P., Friedlingstein, P., Gillett, N., Gregory, J. M., Hartmann, D. L., Jansen, E., Kirtman, B., Knutti, R., Kumar, K. K., Lemke, P. et al (2013) Technical summary. In: Climate Change 2013: The Physical Science Basis. Cambridge
900   University Press. ISBN 9781107661820

Stolzenburg, D., Fischer, L., Vogel, A.L., Heinritzi, M., Schervish, M., Simon, M., Wagner, A.C., Dada, L., Ahonen, L.R., Amorim, A. and Baccarini, A.: Rapid growth of organic aerosol nanoparticles over a wide tropospheric temperature range. Proceedings of the National Academy of Sciences, 115, 9122-9127, doi.org/10.1073/pnas.1807604115, 2018.

905

Twomey,   S.:   Pollution   and   the   planetary   albedo.   Atmospheric   Environment,   8,   1251-1256, doi.org/10.1016/j.atmosenv.2007.10.062, 1967.

Watson, L.A., Shallcross, D.E., Utembe, S.R. and Jenkin, M.E.: A Common Representative Intermediates (CRI) mechanism
910   for VOC degradation. Part 2: Gas phase mechanism reduction. Atmospheric Environment, 42, 7196-7204, doi.org/10.1016/j.atmosenv.2008.07.034, 2008.

Atmospheric
Chemistry
and Physics
Discussions

§

Wennberg, P.O., Bates, K.H., Crounse, J.D., Dodson, L.G., McVay, R.C., Mertens, L.A., Nguyen, T.B., Praske, E., Schwantes, R.H., Smarte, M.D. and St Clair, J.M.: Gas-phase reactions of isoprene and its major oxidation products. Chemical reviews, 118, 3337-3390,doi.org/10.1021/acs.chemrev.7b00439, 2018.

915

Williamson, C.J., Kupc, A., Axisa, D., Bilsback, K.R., Bui, T., Campuzano-Jost, P., Dollner, M., Froyd, K.D., Hodshire, A.L., Jimenez, J.L. and Kodros, J.K.: A large source of cloud condensation nuclei from new particle formation in the tropics. Nature, 574, 399-403, doi.org/10.1038/s41586-019-1638-9, 2019.

920

Wimmer, D., Buenrostro Mazon, S., Manninen, H.E., Kangasluoma, J., Franchin, A., Nieminen, T., Backman, J., Wang, J., Kuang, C., Krejci, R. and Brito, J., 2018. Ground-based observation of clusters and nucleation-mode particles in the Amazon. Atmospheric Chemistry and Physics, 18,13245-13264, 10.5194/acp-18-13245-2018, 2018.

925 Utembe, S.R., Cooke, M.C., Archibald, A.T., Jenkin, M.E., Derwent, R.G. and Shallcross, D.E.: Using a reduced Common Representative Intermediates (CRIv2-R5) mechanism to simulate tropospheric ozone in a 3-D Lagrangian chemistry transport model. Atmospheric Environment, 44, 1609-1622, doi.org/10.1016/j.atmosenv.2010.01.044, 2010.

Xu, L., Møller, K.H., Crounse, J.D., Otkjær, R.V., Kjaergaard, H.G. and Wennberg, P.O.:. Unimolecular reactions of peroxy radicals formed in the oxidation of α-pinene and β-pinene by hydroxyl radicals. The Journal of Physical Chemistry A, 123, 1661-1674, doi.org/10.1021/acs.jpca.8b11726, 2019.

Zhu, J., Penner, J.E., Yu, F., Sillman, S., Andreae, M.O. and Coe, H.: Decrease in radiative forcing by organic aerosol nucleation, climate, and land use change. Nature communications, 10, 423, doi.org/10.1038/s41467-019-08407-7, 2019.

935

Zhao, Y., Thornton, J.A. and Pye, H.O.: Quantitative constraints on autoxidation and dimer formation from direct probing of monoterpene-derived peroxy radical chemistry. Proceedings of the National Academy of Sciences, 48, 12142-12147, doi.org/10.1073/pnas.1812147115,   2018.

940

§
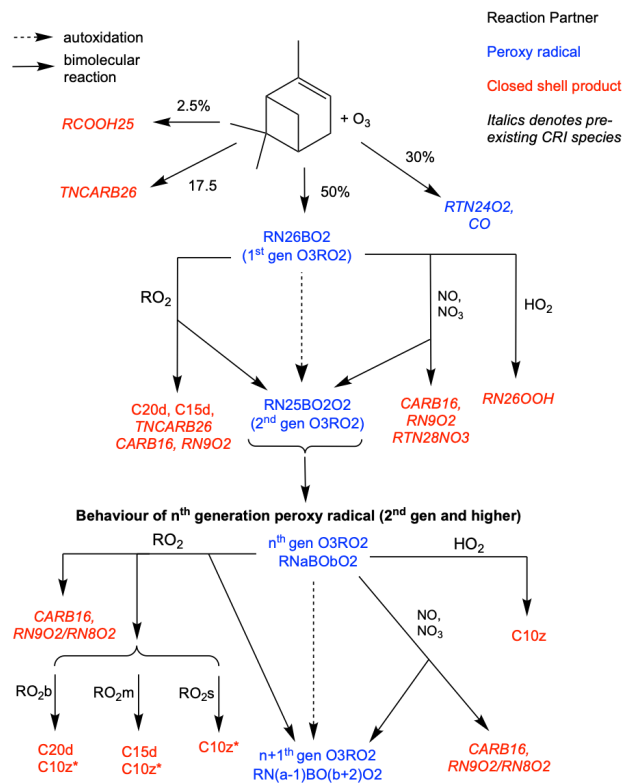
Figure 1: Schematic of additions to CRI v2.2 to represent autoxidation and HOM formation via ozonolysis of α-pinene. HOMs (C10z, C15d, C20d) can be produced via reaction of the O3RO2 with HO₂ and RO₂ while reaction with NO, NO₃ and RO₂ can produce alkoxy radicals which can fragment or isomerise. New species introduced in this scheme are denoted by normal font, existing species by italics.

945

§
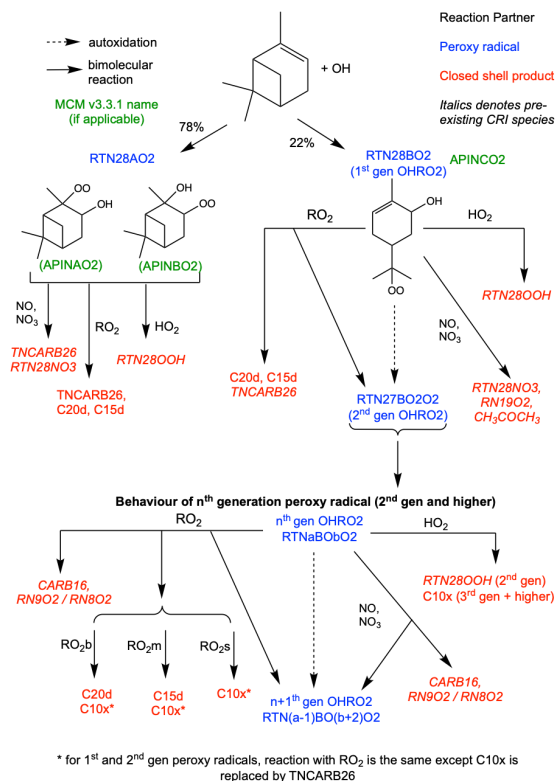
Figure 2 - Schematic of additions to CRI v2.2 to represent autoxidation and HOM formation via OH oxidation. HOMs can be produced via reaction with HO₂ and RO₂ while reaction with NO, NO₃ and RO₂ can produce alkoxy radicals which can fragment or isomerise.

Table 1 - Summary of new species added in HOM mechanism. The removal of species RN18AO2 and RTN28O2 results in a net increase of 12 species.

Species	Classification	Origin	MCM v3.3.1 equivalent
RN26BO2	1st gen peroxy radical	Ozonolysis	C107O2, C109O2
RN25BO2O2	2nd gen peroxy radical	Ozonolysis	Not in MCM
RN24BO4O2	3rd gen peroxy radical	Ozonolysis	Not in MCM
RN23BO6O2	4th gen peroxy radical	Ozonolysis	Not in MCM
RNxBOyO2	Lumped 5th and higher gen peroxy radical	Ozonolysis	Not in MCM
RTN28AO2	1st gen peroxy radical (no autoxidation)	Ozonolysis	APINAO2 and APINBO2
RTN28BO2	1st gen peroxy radical (autoxidation possible)	OH oxidation	APINCO2
RTN27BO2O2	2nd gen peroxy radical	OH oxidation	Not in MCM
RTN26BO4O2	3rd gen peroxy radical	OH oxidation	Not in MCM
RTNxBOyO2	Lumped 4th and higher gen peroxy radical	OH oxidation	Not in MCM
C10z	10-carbon HOM	Ozonolysis	Not in MCM

§

C10x	10-carbon HOM	OH oxidation	Not in MCM
C15d	15-carbon HOM	Ozonolysis and OH oxidation	Not in MCM
C20d	20-carbon HOM	Ozonolysis and OH oxidation	Not in MCM

955

Table 2 - Summary of possible products formed for a particular peroxy radical reacting with the big, medium and small peroxy radical pools.

Size of reacting peroxy radical	Product of reaction with big pool	Product of reaction with medium pool	Product of reaction with small pool
Big (>7 C, e.g. RN26BO2)	C20 HOM accretion product C10 HOM / Existing CRI species* Peroxy radical	C15 HOM accretion product C10 HOM / Existing CRI species* Peroxy radical	C10 HOM / Existing CRI species* Peroxy radical
Medium (4-7 C, e.g. RU14O2)	Closed shell, alkoxy radical		
Small (<4 C, e.g. CH3O2)	Closed shell species, alkoxy radical (no change from CRI v2.2 treatment)		

* The result depends on the extent to which the reacting peroxy radical has been oxidised prior to the RO_2-RO_2 reaction. A

960 HOM is classified as a species which has undergone at least one autoxidation step at atmospherically relevant temperatures and contains at least 6 oxygen atoms (Bianchi et al., 2019). Thus, some of the less oxidised peroxy radicals may not qualify as HOMs and are assigned to the most relevant non-HOM species already in the CRI.

965

970

Table 3 - Simulations used for developing and testing new mechanism

Simulation	Purpose	Mechanism Version(s) Used	Conditions
A: Flow cell experiment	Optimise mechanism by fitting autoxidation coefficients and rate coefficients for accretion product formation	Temperature independent mechanism	297 K, $NO_x < 10^8$ cm^{-3}, dark 26 ppb O_3, initial α-pinene concentration varied
B: Flow cell experiment	Along with Simulation A, optimise mechanism by fitting autoxidation coefficients and rate coefficients for accretion	Temperature independent mechanism	297 K, $NOx < 10^8$ cm^{-3}, dark 80 ppb O_3, 15.6 ppb α-pinene concentration, initial isoprene concentration varied

§

	product formation		
C: Chamber Experiment	HOM yield calculation	Temperature dependent mechanisms with autoxidation activation energies of 6000K, 9000K and 12077K	270 K, 290 K or 310 K α-pinene 15 ppb, O₃ 40 ppb NO, NO₂ varied from 0.01-10 ppb
D: Tropical Boundary Layer Experiment	Compare new mechanism with concentrations predicted by CRI v2.2	Temperature independent and all temperature dependent mechanisms	8 day run with diurnally varying photolysis, temperature (298±4 K), α-pinene and isoprene emissions Multiple runs performed with scaled NO and α-pinene emissions (Full details in SI)

Table 4 - Autoxidation coefficients for the peroxy radicals after fitting to experimental data.

Generation	O3RO2 / s⁻¹	OHRO2 / s⁻¹
1ˢᵗ	0.206	2.1
2ⁿᵈ	1.7	2.1
3ʳᵈ	1.7	0.25
4ᵗʰ	1.6	N/A

975
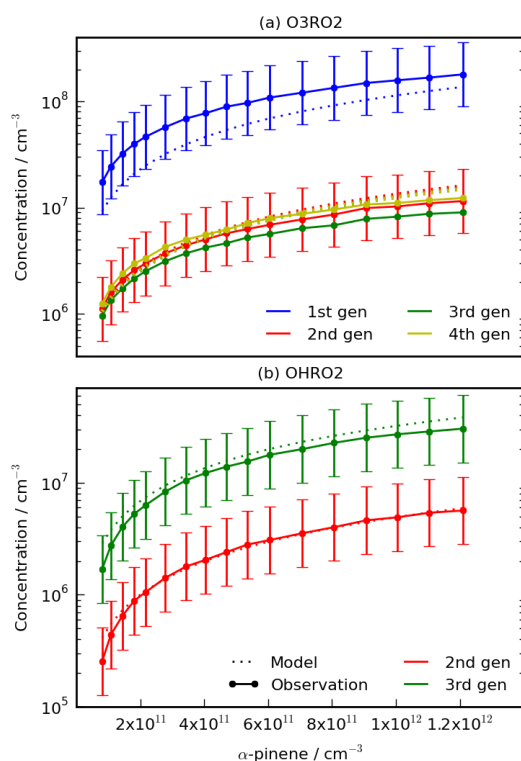
Figure 3 - Comparison of the HOM-precursors (a) O3RO2 and (b) OHRO2 produced by the model and from Berndt et al (2018b) for experiments performed with different initial concentrations of α-pinene (Simulation A). The model reproduces the increase in O3RO2 and 2ⁿᵈ and 3ʳᵈ generation OHRO2 with initial α-pinene well. The model struggled to reproduce concentrations of the 1st generation OHRO2 (not shown).

980

§
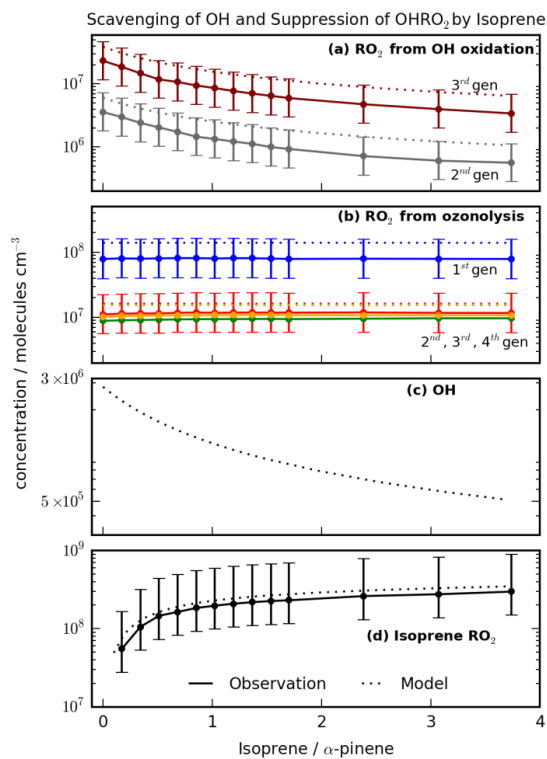
Figure 4 – Observed and modelled variation for Simulation B of OHRO2 (a), O3RO2 (b), OH (c) and the peroxy radical formed from isoprene oxidation (d) with increasing isoprene (observed data from Berndt et al (2018b)). The model is able to reproduce the decrease in OHRO2 as well as their concentrations. The fractional decline of OHRO2 mirrors that observed in the OH concentration, suggesting the major driver is OH scavenging.

985

§
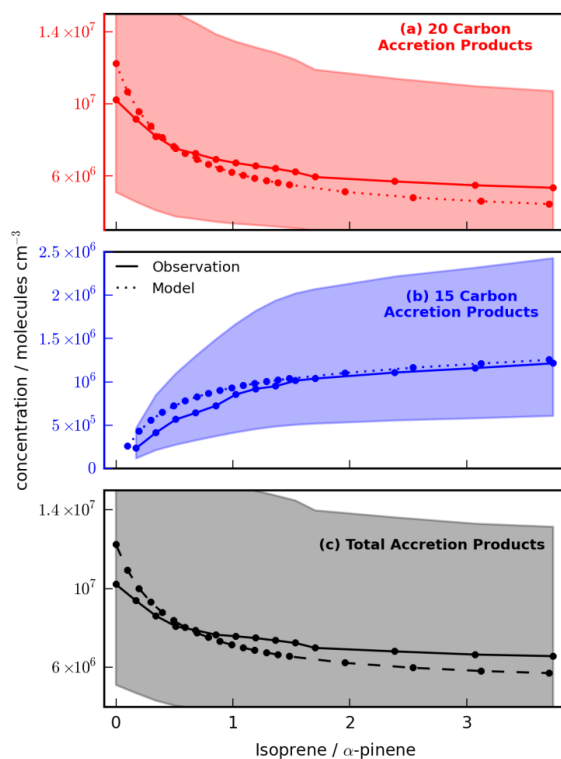
Figure 5 – Variation in Simulation B of observed and modelled concentrations of C20d (a), C15d (b) and total accretion products (c) with isoprene at fixed initial concentrations of α-pinene (observed data from Berndt et al (2018b)). The modelled data falls within the experimental uncertainty shown by the pale red, blue and grey regions. The model reproduces the observed decrease in C20 accretion products and increase in C15 accretion products well. Furthermore, the model reproduces qualitatively the result observed by McFiggans et al (2019) that addition of isoprene reduces the total accretion products concentration with potentially important implications for total aerosol burden and particle size distribution.
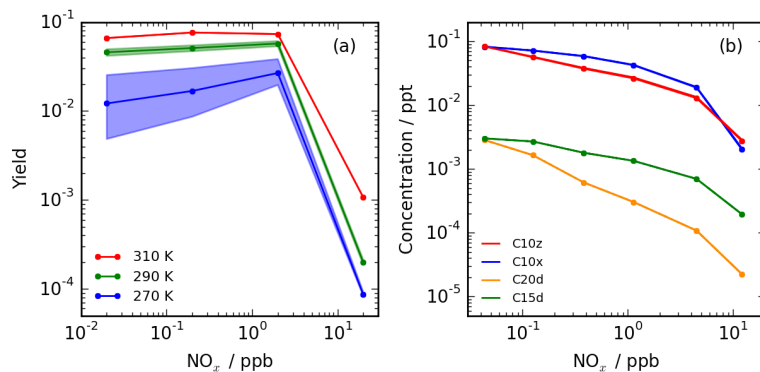
990

Figure 6 – (a) Maximum modelled HOM yields (C10x and C10z) exhibiting significant decline under high NOₓ conditions (Simulation C). The spread in the modelled yield between HOM mechanisms (HOM₆₀₀₀, HOM₉₀₀₀ and HOM₁₂₀₇₇), shown by the shaded regions, indicates the low sensitivity to autoxidation activation energy at temperatures above ~290 K. (b) Observed HOM concentrations from 8 day tropical PBL run (Simulation D) showing decrease in concentration for all HOM species with NOₓ. Under tropical PBL conditions, negligible difference was observed between HOM mechanisms due to daytime temperatures exceeding 300 K.

995

Figure 6 – (a) Maximum modelled HOM yields (C10x and C10z) exhibiting significant decline under high NOₓ conditions (Simulation C). The spread in the modelled yield between HOM mechanisms (HOM₆₀₀₀, HOM₉₀₀₀ and HOM₁₂₀₇₇), shown by the shaded regions, indicates the low sensitivity to autoxidation activation energy at temperatures above ~290 K. (b) Observed HOM concentrations from 8 day tropical PBL run (Simulation D) showing decrease in concentration for all HOM species with NOₓ.

1000 **Under tropical PBL conditions, negligible difference was observed between HOM mechanisms due to daytime temperatures exceeding 300 K.**

Table 5 - Observed and modelled concentrations after adjustment of model input. The model performs well in comparison to observed [HOM] at Hyytiala.

§

Location	Species Adjusted to Observations	Mean observed concentrations at relevant time of day / ppt[e]	Model concentrations with input adjusted to observations / ppt[e]
Hyytiala[a]	Monoterpene	10-carbon HOM: 0.2-0.8 ppt (mean 0.4 ppt) 20-carbon accretion product: 0.04-0.16 ppt (mean 0.08 ppt)	10-carbon HOM: 0.33-0.37 ppt 20-carbon accretion product: 0.18-0.19 ppt
Alabama[b]	Monoterpene, Isoprene, OH, O3	C9 & C10[d]: 30 ppt	C10[f]: 8.0-12.1

1005 [a]*Roldin et al., 2019, [b]Lee et al., 2016, [c]Ranges given accounts for factor of 2 uncertainty in observed concentrations, [d]Includes concentrations from C9 species (C9H14-20O4-10) and C10 species ($C_{10}H_{16-22}O_{4-10}$), [e]Model was run with surface conditions in May for comparison to data from Roldin et al (2019). [f]Range arises from model runs using range of CS values suggested in Lee et al (2016)*
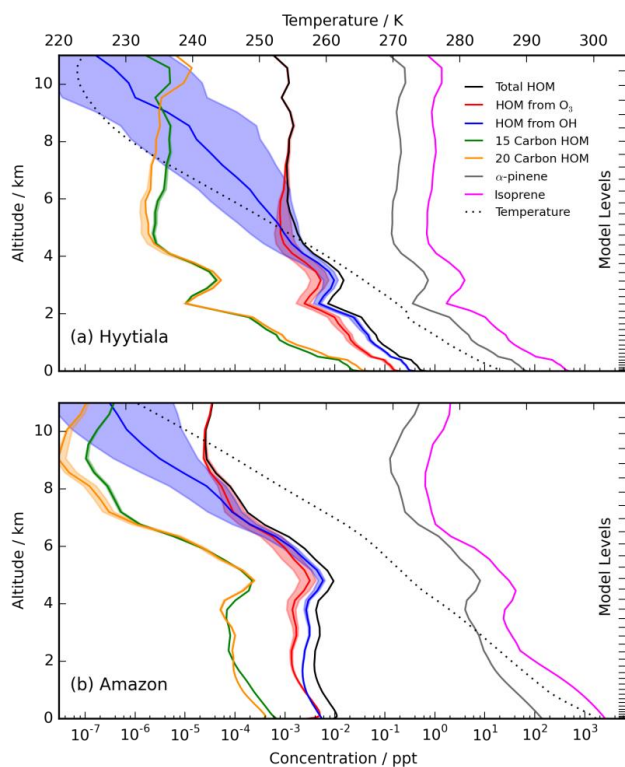
1010 **Figure 7 - HOM profiles in June (2pm LT) above (a) Hyytiala and (b) the Amazon near Manaus. Despite higher [α-pinene], the significantly higher CS in the Amazon results in lower [HOM]. The temperature dependence (shown by the shading) is more significant at low altitude with Hyytiala's cooler temperatures. In (a) the reasonable performance of the model is shown by the overlap of the upper inward-facing arrows (total modelled surface concentrations for 10-carbon HOMs (red) and 20-carbon accretion products (black)) and the lower outward-facing arrows (mean observed surface concentrations). The Amazon's higher**
1015 **isoprene/ α-pinene ratio (~20) resulted in greater suppression of the 20-carbon accretion product than at Hyytiala.**

§
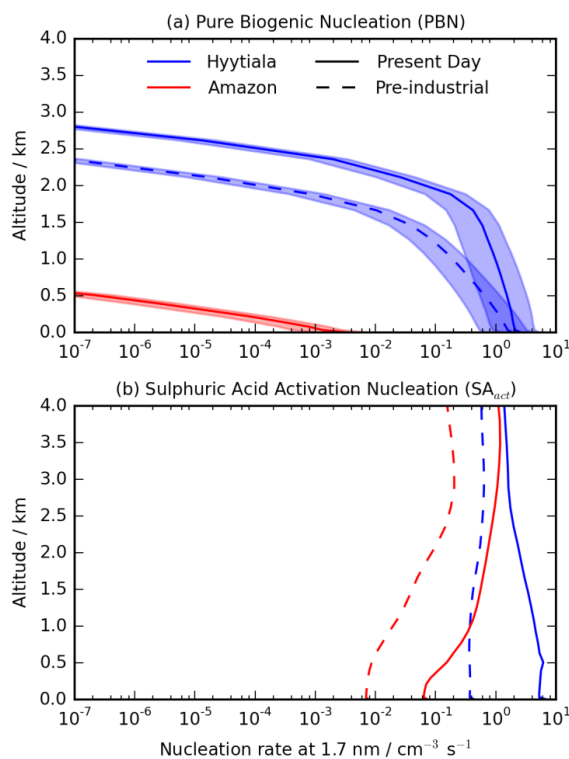
Figure 8 - PD and PI modelled nucleation rates averaged over June for (a) summed (neutral + ion-induced) pure biogenic nucleation (assumes altitude-independent ion production rate (IPR) of 2 cm^{-3} s^{-1} (Hirsiko et al., 2011), shading shows IPR variation 0.5-5 cm^{-3} s^{-1}) and (b) nucleation from sulphuric acid only (SA$_{act}$). Both mechanisms are predicted to produce greater nucleation rates in the PD due to greater concentrations of precursor species. Importantly however, PBN at low altitude at Hyytiala is predicted to be comparable to SA nucleation in the PI due to the greater modelled ion concentration arising from a lower condensation sink and reduction in rates from SA$_{act}$ due to lower sulphuric acid concentrations. This leads to a larger increase in the total nucleation rate in the PI than the PD with potential implications for PI aerosol burden and climate.